# Host–Guest Interactions and Redox Activity in Layered Conductive Metal–Organic Frameworks

Robert M. Stolz<sup>†</sup>, Akbar Mahdavi-Shakib<sup>‡</sup>, Brian G. Frederick<sup>‡\*</sup>, Katherine A. Mirica<sup>†\*</sup>

†Department of Chemistry, Dartmouth College, Hanover NH 03755

Department of Chemistry and Frontier Institute for Research in Sensor Technology (FIRST), University of Maine, Orono ME 04469

**ABSTRACT:** This paper describes the identification of specific host–guest interactions between basic gases (NH<sub>3</sub>, CD<sub>3</sub>CN, and pyridine) and four topologically similar 2-dimensional (2D) metal–organic frameworks (MOFs) comprising copper and nickel bis(diimine) and bis(dioxolene) linkages using diffuse reflectance infrared Fourier transform spectroscopy (DRIFTS), X-ray photoelectron spectroscopy (XPS), electron paramagnetic resonance spectroscopy (EPR), and powder X-ray diffraction (PXRD). This contribution demonstrates that synthetic bottom-up control over surface chemistry of layered MOFs can be used to impart Lewis acidity, or a mixture of Brønsted and Lewis acidities, through the choice of organic ligand and metal cation. This work also distinguishes differences in redox activity within this class of MOFs that contribute to their ability to promote electronic transduction of intermolecular interactions. Future design of structure–function relationships within multifunctional 2D MOFs will benefit from the insights this work provides.

### INTRODUCTION

Layered two-dimensional (2D) conductive metal-organic frameworks (MOFs) have been recently developed as porous multifunctional graphene analogs (Figure 1).1-2 Tunable morphology,3 redox activity,4 and excellent conductivity<sup>1</sup> have made it possible to utilize electronic transduction and activation of these materials within solid-state devices to achieve energy storage,5 charge transport,6-7 electrocatalysis,8 gas sequestration,9 and chemical sensing.1,10-15 These demonstrations of functional performance take advantage of intrinsic design aspects of conductive MOFs that confer multifunctionality from bottom-up synthesis of modular components. The causal link between individual structural components and bulk properties has established precedent for design aspects of porosity, 16-17 conductivity, 2, 18 and crystal packing.1 However, a similar conceptual link between the structural constituents and surface chemistry has not been established. An improved understanding of surface chemistry and accessible host-guest interactions, as well as control of these characteristics by synthetic bottomup means, is required to achieve strategic design of this class of materials towards targeted applications. The ability to synthetically dictate reactivity of surfaces is a significant challenge in the field of 2D materials. The class of MOFs studied in this work offers an opportunity to obtain insight into the issue of controlled surface chemistry.<sup>19</sup>

Recently, Rubio-Giménez et al. described the origin of the chemiresistive response within thin films of Cu<sub>3</sub>(HHTP)<sub>2</sub> MOF.<sup>20</sup> Using infrared reflection absorption spectroscopy (IRRAS), the authors proposed direct interaction of NH<sub>3</sub> gas with Cu<sup>II</sup> centers within the MOF. Kelvin probe microscopy, and computational techniques suggested that Cu<sub>3</sub>(HHTP)<sub>2</sub> underwent a decrease in work function of 0.15 eV upon NH<sub>3</sub>

binding. Computational studies suggested a concomitant increase in the  $\pi\text{-}\pi$  stacking distance upon exposure to NH3, which the authors confirmed by powder X-ray diffraction (PXRD). While previous work provides an insight into the nature of the chemiresistive response of Cu3(HHTP)2 to NH3, the unique role of the constituent ligand and metal center in determining the resulting surface chemistry and redox activity within this class of materials remains entirely unexplored.

This paper describes spectroscopic characterization of the surface chemistry and host-guest interactions of layered conductive MOFs prepared with rod-like morphology based on hexatopic triphenylene ligands complexed with transition metal cations of copper or nickel. The components consist of organic ligands, 2,3,6,7,10,11-hexaaminotriphenylene hydrochloride (HATP•6HCl) or the hydroxy analogue 2,3,6,7,10,11-hexahydroxytriphenylene. which upon complexation with ammoniacal metal cations become 2,3,6,7,10,11-hexaiminotriphenylene (HITP) and deprotonated 2,3,6,7,10,11-hexahydroxytriphenylene (HHTP), to generate the corresponding MOFs: Cu<sub>3</sub>(HITP)<sub>2</sub>, Cu<sub>3</sub>(HHTP)<sub>2</sub>, Ni<sub>3</sub>(HITP)<sub>2</sub>, and Ni<sub>3</sub>(HHTP)<sub>2</sub>.<sup>7, 15, 21</sup> These MOFs all form extended porous sheets having honeycomb *hcb* topology. Yet they differ in their stacking pattern. Cu<sub>3</sub>(HITP)<sub>2</sub>, Ni<sub>3</sub>(HITP)<sub>2</sub>, and Cu<sub>3</sub>(HHTP)<sub>2</sub> crystallize as stacked layers of extended porous sheets, whereas Ni<sub>3</sub>(HHTP)<sub>2</sub> forms as alternating layers of Ni<sub>3</sub>(HHTP)<sub>2</sub> extended sheets and intercalated layers consisting of discrete hydrated Ni<sub>3</sub>(HHTP) complex ions. The complete stoichiometric structure of Ni<sub>3</sub>(HHTP)<sub>2</sub> is provided in the Supporting Information: Section V.7,11,14,21-22 We utilize these four chemically distinct, yet structurally similar, MOFs (Figure 1) to systematically probe the effect of ligand and metal center on the interactions of these host materials with basic gaseous probes (NH<sub>3</sub>, acetonitrile, pyridine). The combined use of diffuse reflectance infrared Fourier transform spectroscopy (DRIFTS), X-ray photoelectron spectroscopy (XPS), electron paramagnetic resonance (EPR) spectroscopy, and PXRD enables characterization of changes in surface chemistry, intermolecular interactions, and redox activity triggered by analytes on the surface of 2D MOFs.

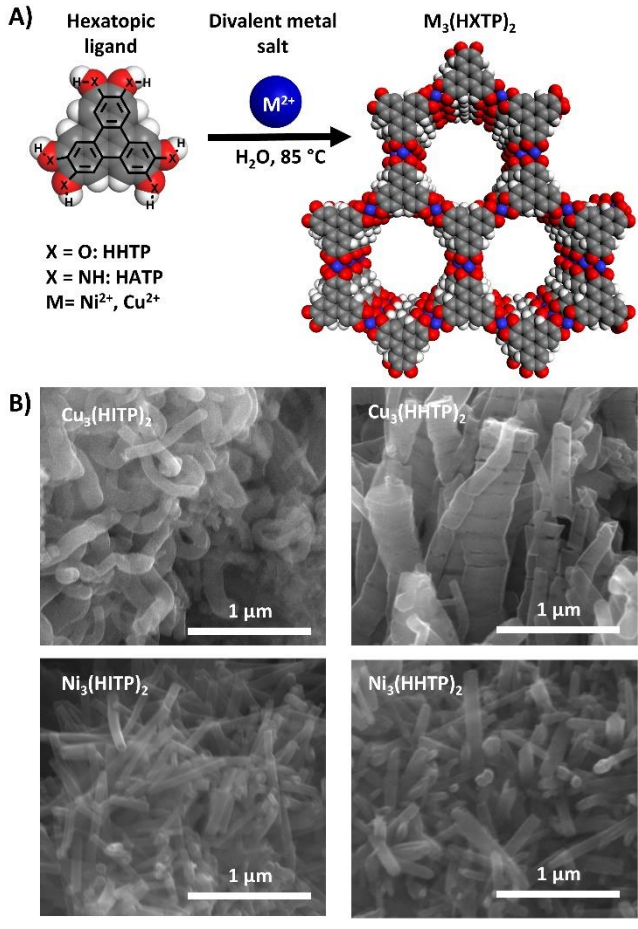


**Figure 1.** Reaction scheme showing the molecular building blocks used to make 2D conductive MOFs and resulting layered hexagonal porous nanostructure of the general formula  $M_3(HXTP)_2$ . (A) The metal centers are shown in blue while heteroatoms are shown in red. Four distinct MOFs with unique characteristics can be generated by the combination of one of two representative ligands 2,3,6,7,10,11-hexahydroxytriphenylene (HHTP) and 2,3,6,7,10,11-hexaiminotriphenylene (HATP), and two representative metals  $Cu^{II}$  and  $Ni^{II}$ . (B) SEM characterization of all four  $M_3(HXTP)_2$  MOFs shows rod-like morphology.

Our work illustrates that the identity of both organic ligand (HHTP vs HITP) and metal center (Cu vs Ni) establish two distinct characteristics of the MOFs: surface acidity and redox activity. First, the ligand controls the surface acidity of MOFs, with Lewis acidity dominating HITP-based MOFs and a combination of Brønsted and Lewis acidity being prevalent for HHTP-based MOFs during interactions with basic probes. Second, exposure of Cu-based MOFs to NH<sub>3</sub> alters the relative population of Cu<sup>II</sup>/Cu<sup>I</sup> by altering the redox balance between Cu nodes and non-innocent ligands, while exposure of Ni-based MOFs to the same analyte induces no detectable change to the redox state of the MOF components. These findings suggest that the strong chemiresistive

response of Cu-based MOFs towards  $NH_3$  previously observed by  $us^{13,23}$  and others  $uspace{11,13,15,23-24}$  is characterized by a combination of Lewis acid/Brønsted acid interactions and a simultaneous change in the redox state of the Cu constituents. Furthermore, a lack of observed chemiresistive response of Ni-based MOFs towards  $uspace{11,13,15}$  is characterized by weak Lewis acid interactions and no change of redox state of the metal center.  $uspace{13,15,23}$ 

### **EXPERIMENTAL DESIGN**

Choice of Metal-Organic Frameworks. 2D conductive MOFs possess several unique properties in the context of chemical sensing: i) porosity; ii) bottom-up tunability in both structure and composition; iii) redox activity. 1, 10 These attributes provide benefits towards different aspects of chemical sensing, such as i) high surface area, ii) possibility of rational design, and iii) redox-based transduction of chemical binding events.<sup>1, 10</sup> To improve understanding of the interplay of these attributes towards improved chemical sensing, accurate knowledge of specific host-guest interactions is required. In this study, we chose to focus on a class of layered 2D MOFs composed of two triphenylenebased organic linkers (either HHTP or HITP) with distinct acidity and two first-row transition metal centers (Cu or Ni) that possess stable +2 oxidation states.<sup>7, 15, 21</sup> In combination, these starting materials can generate four distinct MOFs with unique environments surrounding metal centers (Figure 1, Figure 2).

We hypothesized that comparing the resulting structures and properties of the MOFs shown in **Figure 1** would provide insight and decouple the contributions of distinct chemical components on the host–guest chemistry of 2D MOFs (**Figure 2**). These MOFs can be readily obtained as nanorods (**Figure 1**, **Figure S2-S5**) from aqueous solutions of copper perfluoroacetoacetonate or nickel acetate and appropriate ligand using solvothermal synthetic conditions. Of the four MOFs (collectively referred to as  $M_3(HXTP)_2$ ),  $Cu_3(HITP)_2$ ,  $Ni_3(HITP)_2$ , and  $Cu_3(HHTP)_2$  crystallize as stacked layers of extended sheets (**Figure S6A**), whereas  $Ni_3(HHTP)_2$  forms as alternating layers of  $Ni_3(HHTP)_2$  extended sheets and intercalated layers consisting of discrete  $Ni_3(HHTP)$  complex ions (**Figure S6B**).<sup>7, 11, 15, 21</sup>

The structures of layered MOFs possess at least three distinct types of surfaces that can interact with the surrounding chemical environment. First, the leading edges can be composed of either terminal ligand heteroatoms or may be capped with metal ions. These edge-type functionalities may have exposed metal positions that are coordinatively unsaturated sites (CUS) acting as Lewis Acid Sites (LAS) or may be occupied by aqua ligands, which may act as Brønsted Acid Sites (BAS). Second, the basal plane contains planar ligand-metal-ligand complexes that may act as LAS or BAS depending on degree of hydration. Third, interior pore walls contain exposed ligand heteroatoms and aromatic C-H of the ligands. The case of unique stacking patterns can exist, which lead to additional surface chemistry such as the case of Ni<sub>3</sub>(HHTP)<sub>2</sub>, which possesses an intercalated layer, as mentioned previously. Additional reactive mechanisms at the pore interior may involve radical density that is centered on the carbon portion of the ligand framework for both HITP-based and HHTP-based MOFs.25 The ratio of populations of edge:surface:pore host sites can change as 2D monolayers stack to form crystalline solids.

Molecular-level understanding of the proposed host sites was constructed considering synthetic parameters and literature precedent. First, we endeavored to understand structural and compositional constraints on the set of potential coordination environments that may act as hostsites. These constraints were compiled from a careful analysis of available and proposed crystal structures of the stacked 2D materials, chemical composition of each MOF, as well as the agueous environment used to synthesize the MOFs.<sup>1-3,7,14,20-22,24,26</sup> Our proposition that edge sites may be terminated with hydrated metal nodes (Figure 2A) is based on chemical understanding of metal-catecholate complexes, coupled with the fact that the synthetic conditions used in the synthesis of this family of 2D MOFs relies on stoichiometric excess of metal salts (Supporting Information: Section II).25, 27 Metal-catecholate chemistry has also been demonstrated by Farha and coworkers in the post-synthetic heterogeneous functionalization of MOFs decorated with catecholate groups by exposing solid-phase MOFs to solutions of copper salts.<sup>27</sup> Similar chemistry has also been demonstrated with bidentate nitrogen chelators for postsynthetic metalation of MOFs.<sup>28</sup> These studies demonstrate that dangling catecholate groups in solid materials can readily chelate copper ions from solution. Additionally, these studies show that solid-state copper-catecholate complexes have labile redox structures that can shift between Cull and Cul.

We then considered potential metal-aqua geometries and hydration numbers. Precedent for metal complexes possessing coordinately unsaturated sites, while less common for small molecule complexes, has been a design feature of interest in MOFs.<sup>26, 29-30</sup> Complexes have also been reported with metal sites capped with aqua ligands or solute molecules.<sup>25, 31-32</sup> The result of our examination of experimental constraints and literature precedent lead us to the hypothesis that the terminal edges and basal plane of the layered 2D system examined here would be rich in host-site chemistries following the motifs depicted in **Figure 2A**.

Herein, we have chosen to characterize the surface chemistry of strictly rod-like morphologies because this morphology is readily prepared using simple hydrothermal methods.

Choice of Spectroscopic Characterization Techniques. Four types of spectroscopic techniques were employed to characterize MOF structure, the identity of host sites within the framework, and perturbations induced by host-guest interactions. DRIFTS, XPS, EPR, and PXRD each provided unique information that together was used to obtain comprehensive insight into the nature of host-guest interactions in this class of MOFs.

DRIFTS is an infrared Fourier transform technique that is ideal for characterization of solid-state surface chemistry because it requires minimal sample preparation (e.g., grinding, pressing, high vacuum) typically seen in other methods of IR spectroscopy<sup>33</sup> and is well suited for the in-situ study of surface chemistry by coupling spectroscopy with simultaneous gas exposure at ambient pressure after evacuation.<sup>33</sup>

**Figure 2.** The diversity of potential host sites exhibited by the metal bis(diimine) and metal bis(dioxolene) linkages is outlined (**A**). On both the basal plane and edge facets, host sites may interact with gases as either Brønsted or Lewis acid sites. The basic probe (**B**) gases used in this study are listed with their respective pK<sub>b</sub> and donor number (DN) values indicating the relative strength of their interaction as H-bond acceptors (pK<sub>b</sub>) or with the Lewis acid SbCl<sub>5</sub> (DN).

DN = 33 kcal/mol DN = 59 kcal/mol

DN = 14.1 kcal/mol

The technique has been used to characterize polymer films, 34 catalytic surfaces and processes, 35-38 chemiresistive sensors, 39 and porous materials. 32 The increase or decrease of bands in DRIFTS at characteristic frequencies can reveal the formation or breakage of chemical bonds, while frequency shifts indicate changes in strength or environment. In addition, changes in the population of electronic states in semiconductors lead to broad background absorption. 40 MOF samples were gently combined with powdered KBr to dilute the material and ensure good signal to noise ratio in the DRIFTS experiments (Supporting Information: Section VII). Samples were dried either by vacuum or under a stream of dry Ar.

XPS is a surface-sensitive (<10 nm sampling depth<sup>41</sup>) spectroscopic technique that we used to confirm the elemental composition of the MOF materials as well as chemical shifts typically associated with formal oxidation states(e.g., Cu<sup>0</sup>, Cu<sup>I</sup>, Cu<sup>II</sup>), <sup>32</sup> We analyzed the surface of the MOF in both the pristine state and after exposure to analytes to gain insight into possible redox processes involving framework constituents (i.e., metal center, hexatopic triphenylene ligand, aqua ligands) motivated by the presence of analyte. Because XPS is performed under high vacuum conditions, weakly bound species may desorb. The surface species observed by XPS, therefore, are likely to be the more strongly bound species under ambient conditions. To assess the reproducibility of the XPS measurements, MOF samples were synthesized in triplicate and, therefore, the uncertainty in XPS peak area ratios represent all contributions from synthesis and measurement. For the gas exposure studies undertaken in this work, determination of absolute populations of species by XPS is more complex (vide infra), and, therefore, we only focus primarily on relative comparisons.

EPR spectroscopy is used to observe unpaired electrons and identify their immediate magnetic surroundings as governed by the Zeeman effect, spin-orbit coupling, and nuclear spin coupling.<sup>42</sup> EPR can be used to determine the geometry of EPR-active metal centers and can be used to determine the presence of paramagnetic species as constituents within materials.<sup>43</sup> EPR is complementary to XPS in this work: (1) EPR spectra can be collected at ambient pressure which helps ensure that characterization of adsorbed gases accurately reflects the total adsorption of weakly bound species; and (2) EPR can characterize changes in oxidation state throughout the bulk volume of the sample offering a quantitative view. In this study, we use EPR to observe the effect of gas binding on the location and population of unpaired spins, and changes in oxidation state of metal and ligand constituents. (3) EPR can allow observation of bulk effects. The highly porous MOF materials may allow gas diffusion into the interior of the MOF structure where XPS is not effective.

PXRD is a powerful X-ray diffraction method for interrogating the structure of crystalline materials.<sup>44</sup> Diffraction patterns from powder samples provide information on crystallinity, crystal lattice parameters, and crystal phase identification in a manner that is non-destructive.44 Using Braggs Law, individual diffraction peaks can be converted to diffraction plane spacing which correlate with specific intermolecular distances. 45-46 The accuracy of the technique is highly sensitive to small changes in structure and intermolecular distances within crystal unit cells.<sup>47</sup> The penetration depth of the X-ray beam depends on the material investigated and the experimental technique employed. 45-46 In this work, PXRD is used to for two primary purposes. *First*, the technique is used to confirm the structure of the materials and ensure that samples were free of metal oxide contaminants. Second, the technique was used to analyze the crystalline structure of the materials for small changes that resulting from interactions with basic gases. Generally, for nanomaterials such as those investigated in this paper, PXRD investigates bulk material structure.

Choice of Gaseous Probe Molecules. We chose to probe MOF surface chemistry and host–guest interactions using a class of basic spectroscopic probes of varying pK<sub>b</sub> values: NH<sub>3</sub>,<sup>48-49</sup> pyridine (pyr),<sup>50</sup> and CD<sub>3</sub>CN (**Figure 2**).<sup>51-52</sup> Basic probe gases were chosen due to recent reports that demonstrate the sensitivity of the topical family of MOFs to basic gases such as NH<sub>3</sub> by our group,<sup>13, 23</sup> as well as those of Dincă.<sup>15</sup> Xu.<sup>11</sup> and Martí-Gastaldo.<sup>24</sup>

In chemiresistive sensing, NH<sub>3</sub> is a reducing gas, indicating that the conductivity of n-type semiconductors increases with exposure, while that of p-type semiconductors decreases with exposure.<sup>53</sup> It is a base that typically interacts through a lone pair of sp<sup>3</sup> hybridized electrons.<sup>48</sup> It has been used as a probe molecule for detection of surface acidity for metal oxides,<sup>48,54-55</sup> zeolites,<sup>56-57</sup> and non-conductive *Second*, the region spanning 1200-1600 cm<sup>-1</sup> was assigned to aromatic ring modes and carbonyl modes of triphenylene, and was classified as the aromatic region.<sup>58</sup> MOFs.<sup>32</sup> Interactions between NH<sub>3</sub> and coordinatively

unsaturated surface metal sites are typically described as LAS.<sup>50</sup> When NH<sub>3</sub> interacts with surface hydroxyls, which act as BAS, NH<sub>3</sub> is protonated to NH<sub>4</sub>+ having a local symmetry of C<sub>3v</sub> (**Figure S9**). Characteristic absorbance bands at 1680 cm<sup>-1</sup> and 1450 cm<sup>-1</sup> indicate that NH<sub>3</sub> has been coordinatively bound as NH<sub>4</sub>+.<sup>48</sup>, <sup>55</sup>, <sup>59</sup> Alternatively, NH<sub>3</sub> can also bind to LAS through donation of the basic nitrogen lone pair to an empty or partially filled metal d-orbital resulting in characteristic vibrational modes near 1600 cm<sup>-1</sup> and 1170 cm<sup>-1</sup> that correspond to asymmetric ( $\delta_d$ NH<sub>3</sub>) and symmetric ( $\delta_s$ NH<sub>3</sub>) bending modes, respectively (**Figure S9**).<sup>48</sup>-<sup>49</sup>, <sup>59</sup>-<sup>60</sup> Because ammonia is the strongest base of the probe molecules, it may coordinate to surface aqua ligands or displace them and bond directly with metal centers, resulting in distinct spectral features.

As a probe molecule, CD<sub>3</sub>CN also acts as a Lewis or Brønsted base, but is significantly weaker compared to NH<sub>3</sub>.<sup>51,61</sup> It has been used to distinguish BAS and LAS on surfaces.<sup>62</sup> It can complement the information obtained from the NH<sub>3</sub> probe, because the diagnostic adsorptions near 2300 cm<sup>-1</sup> (LAS >2300 cm<sup>-1</sup>, BAS <2300 cm<sup>-1</sup>) are far removed from the region of IR absorbance bands commonly associated with MOF structures (i.e., carboxylic acid, phenyl, hydroxyl).<sup>51</sup> Perdeuterated CD<sub>3</sub>CN is used to prevent Fermi resonance when CD<sub>3</sub>CN binds to surface sites.<sup>52</sup>

Pyridine can undergo coordination to LAS through the lone pair on the aromatic sp<sup>2</sup> hybridized nitrogen. Alternatively, the nitrogen can be protonated (PyrH<sup>+</sup>) by protic acidic sites such as BAS.<sup>50</sup>

The relative strength of these three nitrogenous basic molecules as Lewis and Brønsted bases allow them to probe a range of surface acidities based on the respective donicity (donor number: DN) and protic acidity. The DN, referring to affinity with respect to SbCl<sub>5</sub>, is strongest for NH<sub>3</sub> (59 kcal/mol) followed by Pyr (33 kcal/mol), and CD3CN (CH<sub>3</sub>CN: 14 kcal/mol, Figure 2).<sup>63</sup> The Brønsted basicity, or proton affinity measured in pKb of the gases follows a similar trend with NH<sub>3</sub> (pk<sub>b</sub> =4.7) being the strongest followed by Pyr (pk<sub>b</sub> = 8.7) and CD<sub>3</sub>CN (CH<sub>3</sub>CN: pk<sub>b</sub> = 18.3, Figure 2).64 We, therefore, anticipated that CD<sub>3</sub>CN would bind to only the strongest acid sites of the MOF, while easily desorbing leaving weaker acid sites undetected. Pyr was expected to bind to weaker acid sites, while NH<sub>3</sub> was expected to interact with the widest range of acid sites. The use of three distinct probes with different binding affinities for LAS sites can enable relative comparisons of Lewis acidity strengths in structurally similar materials.

### **RESULTS AND DISCUSSION**

### Vibrational Spectroscopy of M<sub>3</sub>(HXTP)<sub>2</sub> MOFs.

DRIFTS spectra of pristine MOFs showed three distinct regions of interest (**Figure 3**). *First*, low energy vibrational modes in the range 400-900 cm<sup>-1</sup>, contained metal-heteroatom bond stretching, as well as metal bis(dioxolene), and analogous metal bis(diamine) ring symmetric breathing, and was therefore classified as the metal-ligand region (**Figure 3**).<sup>29</sup>

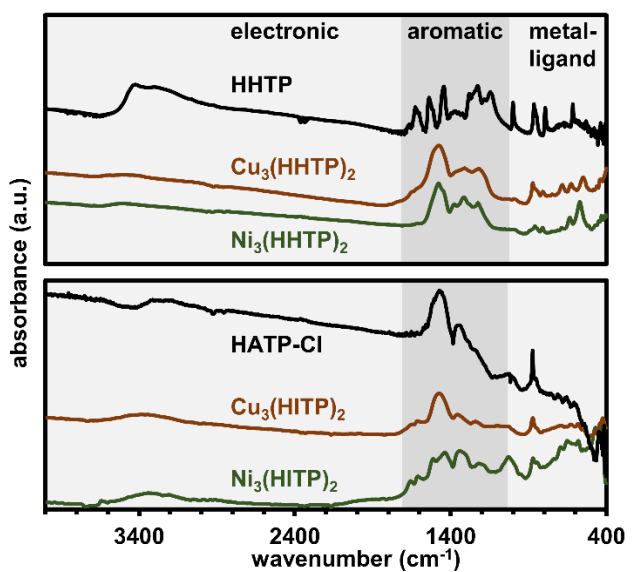


**Figure 3.** DRIFTS spectra of pristine MOFs collected under Ar atmosphere. Distinct regions are delineated by grey shading. The regions are labeled per the dominant features observed in each (see text). **Top**: free HHTP ligand, pristine  $Cu_3(HHTP)_2$  and Pristine  $Ni_3(HHTP)_2$ . **Bottom**: free 2,3,6,7,10,11-hexaaminotriphenylene hydrochloride  $(HATP \bullet 6HCl)$ , pristine  $Cu_3(HITP)_2$ , and pristine  $Ni_3(HITP)_2$ . Spectra have been offset for clarity.

Third, the region >1600 cm<sup>-1</sup>, exhibited a broad baseline absorbance that was determined to be electronic in nature. This baseline electronic absorbance (BEA) could be attributed a combination of the following electronic features: 1) changes in the population of conduction band electrons, 2) the formation of shallow traps, which would allow lowlying transitions to the conduction band (in the mid to near IR range) and 3) charge-transfer reactions consistent with mixed valent systems.<sup>40,65-66</sup> These observations were analogous for all four MOFs in this study (**Figure 3**).

Difference spectra of four MOFs were collected in the presence of 10 % NH $_3$  in He, followed by recovery in an Ar atmosphere (**Figure 4**). The gas-phase bands of ammonia at 3332 cm $^{-1}$  (v $_1$ , a $_1$  asymmetric stretch), 1627 cm $^{-1}$  (v $_4$ , e symmetric bend), and 968/930 cm $^{-1}$  (v $_2$ , a $_1$  symmetric bend) dominated the spectra during exposure, but diminished after purging with inert atmosphere (**Figure S10-S13**).

Exposure of Cu<sub>3</sub>(HITP)<sub>2</sub> to 10% NH<sub>3</sub> in He produced three primary spectral features observable by DRIFTS difference spectra (Figure 4). First, NH<sub>3</sub> produced an initial increase in the BEA from 4000 cm<sup>-1</sup> to 700 cm<sup>-1</sup> (Figure S10). Flushing the system with Ar showed a slow recovery of the BEA (Figure S10B). Second, spectra obtained after exposure showed the formation of new absorption bands at 3332 cm<sup>-1</sup>, 1604 cm<sup>-1</sup>, and 1211 cm<sup>-1</sup> (Figure S10B). Third, negative bands at 3440 cm<sup>-1</sup> and 1654 cm<sup>-1</sup>, formed within 6 min of exposure to NH<sub>3</sub> and persisted upon purging with dry Ar (Figure S10B).

The changes observed in the BEA showed an initial increase in the underlying electronic properties of the material. The specific electronic feature could not be identified from DRIFTS alone. These changes were reversible when NH<sub>3</sub> was removed from the chamber. The strong band at 3332 cm<sup>-1</sup> was attributed to stretching modes of NH<sub>3</sub> that was adsorbed on the material. 55, 59-60, 67 This band did not change from the  $v_1$  spectra of NH<sub>3</sub> in the gas phase and was not characteristic of any specific binding motif of NH<sub>3</sub>; therefore, it was not useful for characterizing interactions between NH<sub>3</sub> and the MOF surface (Figure S10 B). The bands at 1604 cm<sup>-1</sup> and 1211 cm<sup>-1</sup> were assigned to the asymmetric  $\delta_d$  and symmetric  $\delta_s$  vibrational modes of NH<sub>3</sub> adsorbed on LAS (NH<sub>3</sub>-M), respectively (Figure 4, Figure **S9**). 55, 59-60, 67 The negative bands at 3440 cm<sup>-1</sup> and 1654 cm<sup>-2</sup> <sup>1</sup> were attributed to the stretching ( $\nu$ (OH)) and bending  $(\delta(H_2O))$  modes of water, respectively, that was displaced by adsorption of ammonia.65 The observed absorbance bands of the water ligands were in good agreement with literature reports of H<sub>2</sub>O on TiO<sub>2</sub> films.<sup>65</sup>

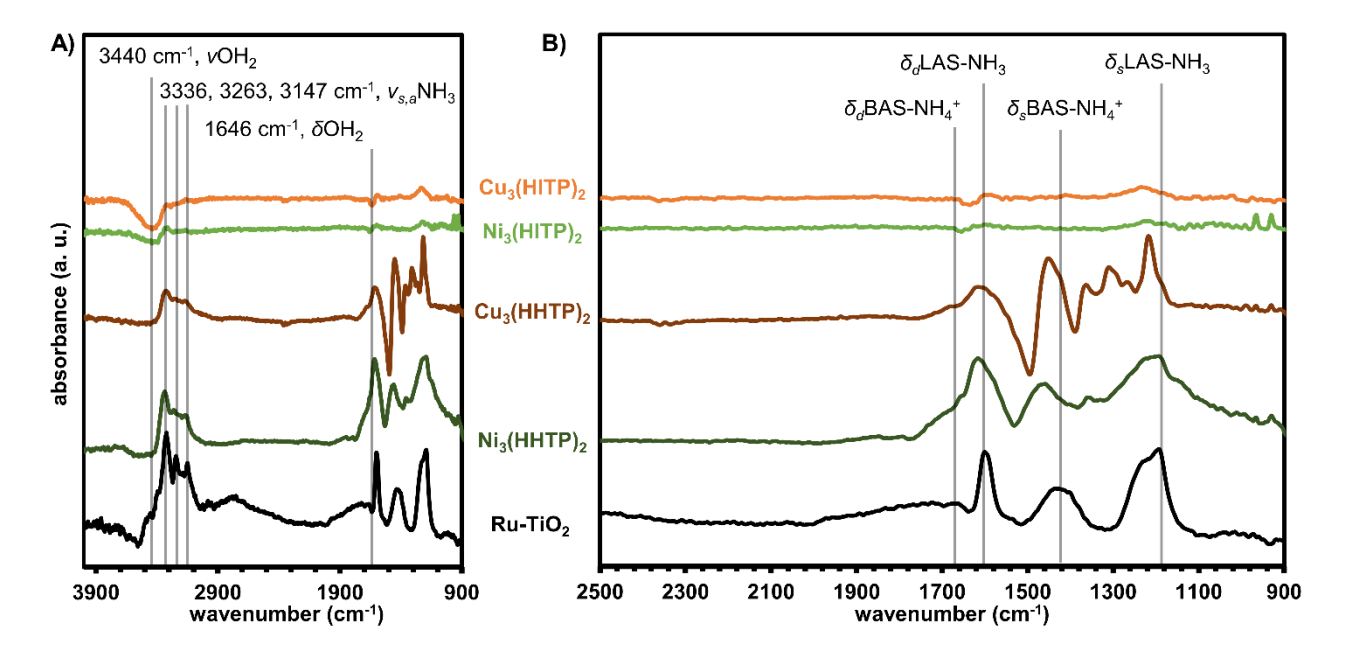


**Figure 4.** DRIFTS difference spectra of MOFs after exposure to 10% NH<sub>3</sub> in He for 6 min, followed by purging with Ar for 12 min to remove residual gas phase NH<sub>3</sub>. **A)** Full spectra of NH<sub>3</sub> on M<sub>3</sub>(HXTP)<sub>2</sub> MOFs with bending and stretching modes of water and NH<sub>3</sub> labeled. The positive bands in the  $\nu$ NH<sub>3</sub> region indicate the presence of NH<sub>3</sub> while the negative bands corresponding to  $\nu$ OH<sub>2</sub> and  $\delta$ OH<sub>2</sub> indicate dehydration of the MOF upon exposure to NH<sub>3</sub>. **B)** expanded spectral region containing characteristic bands of specific binding modes of NH<sub>3</sub> to LAS and BAS. Spectra are compared to well-characterized Ru-TiO<sub>2</sub>+NH<sub>3</sub> exhibiting both LAS and BAS acidity. The exact location of vibrational bands for each MOF are listed in the accompanying **Table 1**.

**Table 1.** Assignment of the vibrational modes observed in the spectra shown in **Figure 4**. The symmetry assignments of the vibrational modes are included in **Figure S9**. Notation: *neg*: negative going band, v: stretching,  $\delta_d$ : asymmetric deformation,  $\delta_s$ : symmetric deformation (umbrella mode), BEA: broad electronic background, rev: reversible; irrev: irreversible.

characteristic vibrational modes (cm <sup>-1</sup> ) and assignments								
$M_3(HXTP)_2$	vOH2 (neg)	$\delta \mathrm{OH_2}(neg)$	$\delta_d \mathrm{NH_4^+ ext{-}BAS}$	$\delta_d$ NH <sub>3</sub> -LAS	$\delta_s$ NH <sub>4</sub> +-BAS	$\delta_s$ NH <sub>3</sub> -LAS	BEA	
Cu <sub>3</sub> (HITP) <sub>2</sub>	3440	1654	-	1604	-	1211	Increase, rev.	
$Cu_3(HHTP)_2$	3440	-	1685	1608	1423	1187	Decrease, rev.	
Ni <sub>3</sub> (HITP) <sub>2</sub>	3440	1654	-	1612	-	1226	Increase, irrev.	
$Ni_3(HHTP)_2$	3440	-	1677	1608	1454	1195	Decrease, irrev.	

Exposure of Cu<sub>3</sub>(HHTP)<sub>2</sub> to 10% NH<sub>3</sub> in He produced three spectral features observable with DRIFTS difference experiments (Figure 4), which were distinct from those obtained for Cu<sub>3</sub>(HITP)<sub>2</sub>. First, in contrast to the increased BAE absorbance observed for Cu<sub>3</sub>(HITP)<sub>2</sub>, NH<sub>3</sub> caused a decrease in the BAE absorbance from 4000 cm<sup>-1</sup> to 1700 cm<sup>-1</sup> for the Cu<sub>3</sub>(HHTP)<sub>2</sub> MOF analog (**Figure S11B**). This BEA shift was partially reversible when NH<sub>3</sub> was purged from the chamber with Ar (Figure S11B). Second, a negative going band was observed at 3440 cm<sup>-1</sup>. Third, spectra obtained after purging the chamber with Ar for 6 min showed absorption bands at 3336 cm<sup>-1</sup>, 1685 cm<sup>-1</sup>, 1608 cm<sup>-1</sup>, 1454 cm<sup>-1</sup>, 1423 cm<sup>-1</sup>(sh.), 1357 cm<sup>-1</sup>, 1315 cm<sup>-1</sup>, 1268 cm<sup>-1</sup>, and 1187 cm<sup>-1</sup> <sup>1</sup>(sh.) (Figure 4, Figure S11B). These bands did not significantly decrease in intensity when the chamber was purged with Ar.

The bands observed near 3336 cm<sup>-1</sup> (Figure 4) were ascribed to stretching modes of NH<sub>3</sub> adsorbed on the surface of the material.55,59-60,67 The shoulder at 1608 cm-1 and the shoulder at 1187 cm<sup>-1</sup> were assigned to the symmetric  $\delta_d$ and asymmetric  $\delta_s$  vibrational modes of NH<sub>3</sub> bound to LAS (NH<sub>3</sub>-M), respectively (Figure 4).<sup>55, 59-60, 67</sup> The band observed at 1215 cm<sup>-1</sup> was assigned to perturbations to aromatic vibrational modes. Likewise, the band at 1454 cm<sup>-1</sup> was asymmetric and was assigned to the vCC+vCO vibrational mode of HHTP shifting towards lower wavenumbers (originally observed at 1477 cm<sup>-1</sup> for the pristine MOF, Figure S18A). The shoulder bands observed at 1685 cm<sup>-1</sup> and 1423 cm<sup>-1</sup> were assigned to  $\delta_d$  and  $\delta_s$  of NH<sub>4</sub><sup>+</sup> resulting from NH<sub>3</sub> participating in hydrogen bonds with BAS on the MOF. respectively.55, 59-60, 67. Finally, the negative going band at 3440 cm<sup>-1</sup> was assigned to the loss of water from the framework upon exposure to NH<sub>3</sub>.

**Exposure of Ni<sub>3</sub>(HITP)<sub>2</sub> MOF to 10% NH**<sub>3</sub> in He produced three distinct spectral features (**Figure 4**). *First*, exposure caused an *increase* in the BAE absorbance from 663 cm<sup>-1</sup> through 4000 cm<sup>-1</sup> (**Figure S12B**). This change in BAE was slow and irreversible and continued to increase when the chamber was purged with Ar (**Figure S12B**). *Second*, we observed new absorbance bands at 3332 cm<sup>-1</sup>, 1612 cm<sup>-1</sup>, and 1226 cm<sup>-1</sup> that persisted when the sample was flushed

with Ar (**Figure S12B**). *Third*, negative absorbance bands were observed at 3440 cm<sup>-1</sup> and 1654 cm<sup>-1</sup> beginning with NH<sub>3</sub> exposure (**Figure S12B**).

The partially reversible decrease of the BEA indicated that there was a decrease in the accountable electronic properties that were only partially recoverable when NH<sub>3</sub> was removed from the chamber. The positive band at 3332 cm<sup>-1</sup> was attributed to the  $v_1$  stretching mode of NH<sub>3</sub> adsorbed on the surface of the material. 55, 59-60, 67 The absorbance band at 1612 cm<sup>-1</sup> was ascribed to the  $\delta_d$  vibrational mode of NH<sub>3</sub> on LAS (M-NH<sub>3</sub>) while the band at 1226 cm<sup>-1</sup> was assigned to the  $\delta_s$  vibrational mode of the same species. 55, 59-60, 67 The negative bands at 3440 cm<sup>-1</sup> and 1654 cm<sup>-1</sup> were attributed to the  $v(\text{H}_2\text{O})$  and  $\delta(\text{H}_2\text{O})$  bands of displaced surface bound water, respectively. Elke, Cu<sub>3</sub>(HITP)<sub>2</sub>, the negative going nature of these bands indicated that water desorbed from the framework with the addition of NH<sub>3</sub>.

Exposure of Ni<sub>3</sub>(HHTP)<sub>2</sub> to 10% NH<sub>3</sub> was observed with DRIFTS difference experiments, which revealed *three* significant features that indicated interactions with the MOF surface (Figure 4). First, exposure to NH<sub>3</sub> caused a decrease in the BAE absorbance from 4000 cm<sup>-1</sup> to 750 cm<sup>-1</sup>. The decrease was fast and was observed to be largely irreversible even under extended purging with Ar (Figure S13B). Second, spectra obtained after purging with Ar showed the formation of intense positive bands at 3336 cm<sup>-1</sup>, 1677 cm<sup>-1</sup>, 1608 cm<sup>-1</sup>, 1454 cm<sup>-1</sup>, 1195 cm<sup>-1</sup>, 829 cm<sup>-1</sup>, 636 cm<sup>-1</sup>, and 609 cm<sup>-1</sup> (Figure S13B). Third, a weak negative going band was observed at 3440 cm<sup>-1</sup> (Figure S13B). These bands did not diminish in intensity when the chamber was purged with Ar for 12 min.

The strong band at 3336 cm<sup>-1</sup> was attributed to the  $v_1$  mode of NH<sub>3</sub> adsorbed on the material (**Figure S13B**).<sup>48, 55, 59-60, 67</sup> The bands at 1608 cm<sup>-1</sup> and 1195 cm<sup>-1</sup> were similar to those observed for Cu<sub>3</sub>(HHTP)<sub>2</sub>+NH<sub>3</sub> and were assigned to the  $\delta_d$  and  $\delta_s$  vibrational modes of NH<sub>3</sub> bound to LAS (M-NH<sub>3</sub>), respectively.<sup>48, 55, 59-60, 67</sup> The bands at 1677 cm<sup>-1</sup> and 1454 cm<sup>-1</sup> was ascribed to the  $\delta_d$  and  $\delta_s$  modes of NH<sub>4</sub><sup>+</sup> on BAS, respectively(**Figure S13B**). The bands at 829 cm<sup>-1</sup>, 636 cm<sup>-1</sup>, and 609 cm<sup>-1</sup> were modes likely originating from M-L

vibrational modes (**Figure S13B**).<sup>48, 55, 59-60, 67</sup> The negative going band at 3440 cm<sup>-1</sup> was ascribed to the  $v(OH_2)$  mode of adsorbed water. The not-observed  $\delta(OH_2)$  band was most likely obscured by the  $\delta_d NH_4^+$ -BAS band.

Exposure of MOFs to CD<sub>3</sub>CN. For the HHTP-based MOFs, peaks diagnostic of NH<sub>3</sub> binding to acidic host sites overlapped with modes assigned to aromatic ring vibrations. This overlap posed a challenge for unambiguously differentiating perturbations stemming from probe-acidic site interactions from perturbations to the backbone ring vibrational frequencies.<sup>69</sup> To overcome this challenge, we selected CD<sub>3</sub>CN as an additional probe because it exhibited characteristic vibrational frequencies (2300-2350 cm<sup>-1</sup>),<sup>61</sup>. <sup>68</sup> which were significantly separated from backbone aromatic ring bands. CD<sub>3</sub>CN also acts as a weaker Brønsted and Lewis base allowing weak acid sites to go undetected.

Adsorption of CD<sub>3</sub>CN gave evidence for the strong Lewis acidity of Ni<sub>3</sub>(HHTP)<sub>2</sub> due to the new band observed at 2310 cm<sup>-1</sup> corresponding to the *v<sub>CN</sub>* mode of CD<sub>3</sub>CN (**Figure 5, Figure S17**). All four of the MOFs displayed a new band at 2260 cm<sup>-1</sup>, which corresponded to the *v<sub>CN</sub>* mode of CD<sub>3</sub>CN adsorbed on either BAS or physisorbed on the surface of the MOF (**Figure 5, Figure S14-S17**). Since this vibrational band was not unique to any specific adsorbed state, the vibrational mode was not definitively assigned. CD<sub>3</sub>CN also induced large perturbations to ring vibrational modes of HHTP-based MOFs (**Figure 5**).

Consistent with the NH<sub>3</sub> data, CD<sub>3</sub>CN did not show strong perturbations of the ring modes of HITP-based MOFs. These MOFs showed LAS that formed when ammonia displaced water. Since CD<sub>3</sub>CN is characterized by a significantly lower pKb value compared to NH3 (Figure 2B), the lack of Lewis acidity observed for Cu<sub>3</sub>(HITP)<sub>2</sub> and Ni<sub>3</sub>(HITP)<sub>2</sub> towards CD<sub>3</sub>CN, but observed towards NH<sub>3</sub> indicated the acidity of their LAS were weaker than Ni<sub>3</sub>(HHTP)<sub>2</sub>. In the case of HHTP-based MOFs, the perturbations to the aromatic region were qualitatively different for the Cu and Ni analogs. The perturbations for Cu<sub>3</sub>(HHTP)<sub>2</sub> were similar to the features observed in the difference spectra after ammonia exposure, but the absence of LAS-bound CD<sub>3</sub>CN suggested that the perturbation of the ring modes with both NH<sub>3</sub> and CD<sub>3</sub>CN involve adsorption at BAS. The results of the comparison are included in the Supporting Information (Figure **S18**).

Exposure of MOFs to Pyr provided further information about the strength of acid sites on HITP-based analogues. Pyr is a basic probe of intermediate Lewis and Brønsted basicity. When compared to the previous probes, Pyr is less basic than NH<sub>3</sub>, but more basic than CD<sub>3</sub>CN. As a Lewis base, Pyr is a better electron donor than CD<sub>3</sub>CN, but weaker than NH<sub>3</sub>. The interaction between Pyr and both HITP-based MOFs was investigated by DRIFTS to determine the importance of probe basicity for interaction involving these two MOFs.

Exposure of Cu<sub>3</sub>(HITP)<sub>2</sub> to gas phase Pyr was observed with DRIFTS difference experiments (**Figure S19A**). Exposure to Pyr caused only two changes to the spectra of the

MOF. *First*, a positive going change to the BEA absorbance across the broad range 4000 cm<sup>-1</sup> to 800 cm<sup>-1</sup> was observed (**Figure S19A**), which was larger in magnitude than for ammonia interacting with LAS of Cu<sub>3</sub>(HITP)<sub>2</sub>. The increase in BEA was only slightly reversible by evacuation of the system. *Second*, the weak bands remaining after evacuation at 1594 cm<sup>-1</sup> and 1454 cm<sup>-1</sup>, were indicative of Pyr binding to LAS (**Figure S20**).

Ni<sub>3</sub>(HITP)<sub>2</sub> showed similar bands when exposed to Pyr, but the bands disappeared upon evacuation (**Figure S19**). This observation indicated the Lewis acid sites on Ni<sub>3</sub>(HITP)<sub>2</sub> were weaker than those on Cu<sub>3</sub>(HITP)<sub>2</sub>. The BEA was observed to decrease in the presence of Pyr and decreased further upon evacuation, similar to the behavior observed for Ni<sub>3</sub>(HITP)<sub>2</sub>+NH<sub>3</sub> (**Figure S19B, Figure S20**).

Surface Chemistry of MOFs Identified by DRIFTS. Characterization of the HITP-based MOFs with basic probe gases yielded two primary results. First, the mode of interaction between basic gases and the surface of Cu<sub>3</sub>(HITP)<sub>2</sub> and Ni<sub>3</sub>(HITP)<sub>2</sub> was primarily through coordination to LAS; for NH<sub>3</sub> this was indicated by the absorbance bands detected near 1608 cm<sup>-1</sup> and 1189 cm<sup>-1</sup> (Figure 4). The acidity of these sites was weak as the response to weakly basic gases such as CD<sub>3</sub>CN showed only physisorption. Pyridine, a slightly stronger basic gas, showed Lewis acidity for Cu<sub>3</sub>(HITP)<sub>2</sub> but only indiscernible interactions with Ni<sub>3</sub>(HITP)<sub>2</sub>. In response to Pyr, the BEA of Cu<sub>3</sub>(HITP)<sub>2</sub> increased and the BEA of Ni<sub>3</sub>(HITP)<sub>2</sub> decreased (Figure S20). We, therefore, conclude that the Lewis acidity of Cu<sub>3</sub>(HITP)<sub>2</sub> was stronger than the Lewis acidity of Ni<sub>3</sub>(HITP)<sub>2</sub>. Second, coordination of NH<sub>3</sub> to LAS coincided with a decrease in the prevalence of surface-bound water for both HITP-based MOFs, as indicated by the observed negative bands attributed to the v(OH) and  $\delta(H_2O)$  bands of adsorbed water, respectively (**Figure 4**). We hypothesize that the weak LAS responsible for coordination of NH<sub>3</sub> were formed as NH<sub>3</sub> displaced water ligands from the MOF. Pvr and CD<sub>3</sub>CN, with weaker DN compared to NH<sub>3</sub>, (Figure 2B) were unable to cause the displacement of water from the surface of HITPbased MOFs. Thus, LAS were not activated, and subsequently not detected, by the CD<sub>3</sub>CN and Pyr probes in HITPbased MOFs.

Characterization of the surface chemistry of the HHTPanalogues [Cu<sub>3</sub>(HHTP)<sub>2</sub> and Ni<sub>3</sub>(HHTP)<sub>2</sub>] revealed three key comparisons with the HITP-based analogues. First, the surface chemistry of the MOFs was observed to be dominated by a mixture of LAS and BAS for Cu<sub>3</sub>(HHTP)<sub>2</sub> and Ni<sub>3</sub>(HHTP)<sub>2</sub>. This was confirmed by specific vibrational modes corresponding to adsorbed NH<sub>3</sub> (Figure 4). Second, the observation of LAS acidity for Ni<sub>3</sub>(HHTP)<sub>2</sub>, but not for Cu<sub>3</sub>(HHTP)<sub>2</sub>, using CD<sub>3</sub>CN probe indicated that Ni<sub>3</sub>(HHTP)<sub>2</sub> hosted stronger LAS than the Cu-analogue (or either of the HITP MOFs). *Third*, we observed a general trend that HHTPbased MOFs appeared to host stronger interactions with NH<sub>3</sub> and CD<sub>3</sub>CN, while HITP-based MOFs showed weaker disruptions to the both the ring modes and the BEA along with less intense absorbance bands corresponding to adsorbed probe (Figure 4-5).

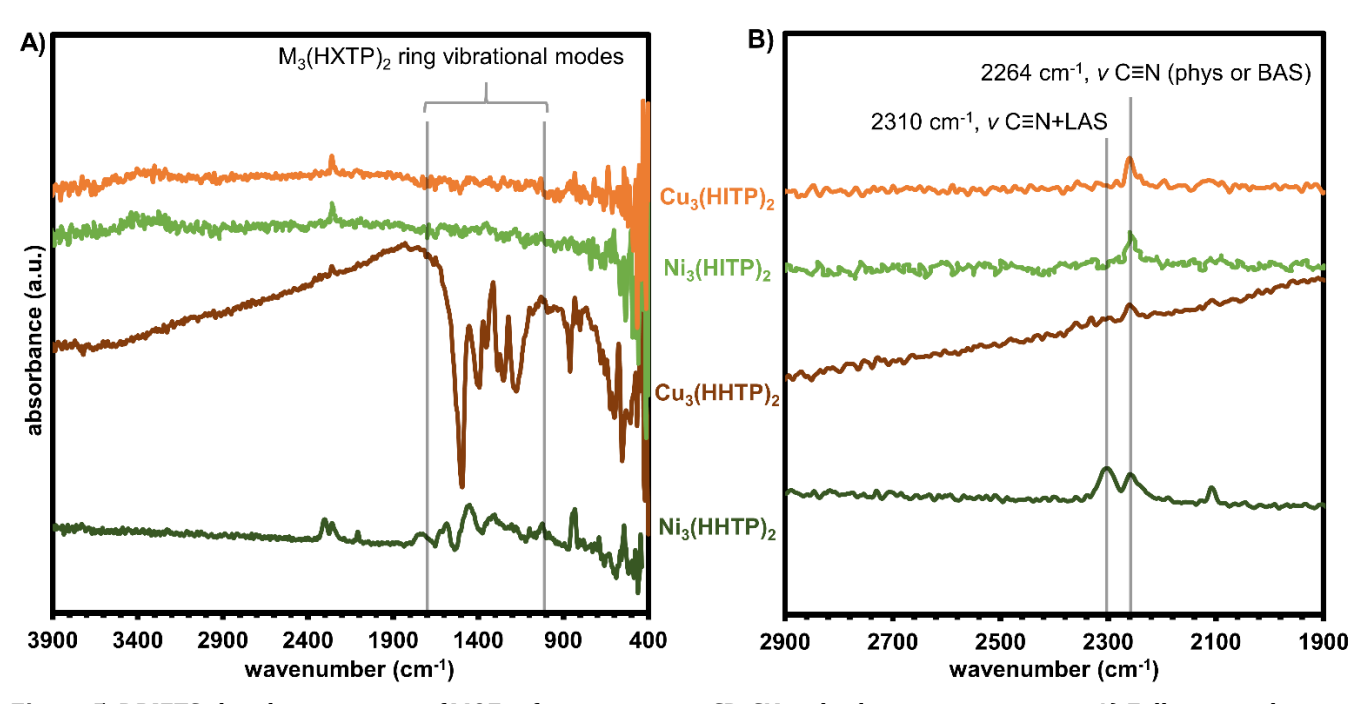


Figure 5. DRIFTS absorbance spectra of MOFs after exposure to  $CD_3CN$  and subsequent evacuation. A) Full spectra showing characteristic region as well as perturbations to the ring vibrational modes. B) expanded region showing detailed labelling of the  $\nu$ C $\equiv$ N region. The three MOFs  $Cu_3(HITP)_2$ ,  $Ni_3(HITP)_2$ , and  $Cu_3(HITP)_2$  displayed weak interactions primarily with BAS or physisorption.  $Ni_3(HHTP)_2$  showed an additional interaction between  $CD_3CN$  and a LAS. Only HHTP-based MOFs showed strong perturbations to ring vibrational modes. Notation: *phys:* physisorption.

Because the basic gas probes were hypothesized to interact with the MOF as reducing agents (from a chemiresistive sensor perspective), the changes in the aromatic IR region of the HHTP-based MOFs observed for interactions with NH $_3$  and CD $_3$ CN suggested that redox shifts were occurring as a result of NH $_3$  adsorption. To probe this, we used XPS to observe the oxidation state of elemental components within the MOFs before and after exposure to the representative probe NH $_3$ .

XPS characterization of MOFs and their exposure to NH<sub>3</sub>. XPS analysis was used to analyze composition of the MOF materials in the pristine state and after exposure to NH<sub>3</sub>. Pristine MOF was used after purging for 24 h with N<sub>2</sub>. Pristine MOF samples were exposed to 1% NH<sub>3</sub> in N<sub>2</sub> for 20 min to yield MOF+NH<sub>3</sub>. XPS analysis was carried out at base pressure of 10-9 Torr, which typically required 0.5 hours of strong evacuation to achieve. It is important to note that this aspect of XPS analysis may promote desorption of water from the surface or desorption of reversible host-guest interactions, leaving only strong or irreversible interactions detectable by this technique. However, because we compare relative differences of pristine and analyte-exposed materials under a similar set of conditions, the use of XPS still provides valuable insight into the structure of these materials. Comparative differences before and after exposure were used to assess three aspects of the MOF surface chemistry and effects of interaction with NH<sub>3</sub> guests: 1) determination of surface functionalities and confirmation of the composition of MOF samples compared to reported values, 2) confirmation of gas binding to the MOF surface (MOF+NH<sub>3</sub>), and 3) investigation into effects resulting from gas binding, as determined by changes in relative populations of surface

species and their oxidation states. XPS experiments consisted of survey spectra encompassing a wide range of photoemission energies, followed by high resolution scans of identified elemental regions.

All four MOFs exhibited elemental photoemission lines in accordance with their proposed structure (Figure S21-**S24**). MOFs composed of HHTP and metal ion showed the presence of the expected metal species, carbon, and oxygen. Deconvolution of the carbon photoemission lines for both M<sub>3</sub>HHTP<sub>2</sub> MOFs revealed multiple environments for carbon corresponding to ring-fused carbons of HHTP at low binding energies, alcoholic carbons of HHTP at higher binding energies, and at the highest binding energies carbonyl carbons of HHTP (Figure S30, S38). Deconvoluted oxygen photoemission lines showed that framework-bound oxygen species originating from HHTP heterolinkers were distinguishable as two separate environments — the more oxidized C=O-M was observed at high binding energies and the reduced C-O-M species at lower binding energies (Figure \$32, \$40). These unique environments for O1s originated from the different oxidation states of HHTP. An additional oxygen environment corresponding to surface bound H<sub>2</sub>O was observed at high binding energies (Figure S32, S40). Analogously, HITP-based MOFs showed strong photoemission lines for the expected elements carbon, nitrogen, and appropriate metal (i.e., Cu or Ni). Deconvolution of the carbon photoemission line revealed carbon environments arising from HITP similar to those found for HHTP-based MOFs (Figure S27, S34). The nitrogen region of Cu<sub>3</sub>(HITP)<sub>2</sub> and Ni<sub>3</sub>(HITP)<sub>2</sub> both showed two environments for nitrogen corresponding to two distinct oxidation states for the bis(diimine) species (Figure S28, S35). The more oxidized C=(HN)-M appeared at higher binding energies and the reduced C-(HN)-M appeared at lower binding energies. The structurally unaccounted-for O1s photoemission line present in both M<sub>3</sub>HITP<sub>2</sub> MOFs was bimodal and was interpreted as the presence of water adsorbed to the framework (**Figure S29, S36**).

The quantification of metal oxidation states in pristine MOFs was accomplished by analysis of metal 2p<sub>3/2</sub> regions (Figure S25, S26, S33, S37). Both Cu containing MOFs showed mixed valences of Cu<sup>I</sup> and Cu<sup>II</sup> in the pristine state. Cu<sub>3</sub>(HITP)<sub>2</sub> showed a distribution of 42% Cu<sup>1</sup> and 58% Cu<sup>11</sup>. while Cu<sub>3</sub>(HHTP)<sub>2</sub> contained a distribution of 16% Cu<sup>1</sup> and 84% Cu<sup>II</sup>. The observation of mixed valency (Cu<sup>II</sup>/Cu<sup>I</sup>) matched previous reports.9, 14 The quantitative mixed valences observed for Cu<sub>3</sub>HXTP<sub>2</sub> did not match distributions previously reported by us and others.<sup>9, 14</sup> However, this work utilized a more quantitative XPS analysis of Cu<sup>II</sup>/Cu<sup>I</sup> distributions by comparing satellite shakeup peak intensity with the intensity of the primary photoemission line for Cu2p<sub>3/2</sub> (Supporting Information Section XII, Method I).70-71 In part this could be due to different preparation methods (e.g. washing procedures, storage procedures, etc.). It is important to note that the pristine state described for these MOFs is after exposure to high vacuum needed for XPS. The high vacuum could alter metal oxidations states as water desorbs from ligand or metal positions.

After obtaining a baseline analysis of the pristine MOFs, we turned our attention to the effects of gas binding by XPS. First, we confirmed that  $NH_3$  binds to the surface of all four MOFs throughout the experiment and is at least partially retained under the high vacuum conditions of XPS. For  $Cu_3(HHTP)_2$  and  $Ni_3(HHTP)_2$  this observation was revealed by a new photoemission line that appeared after exposure to  $NH_3$  (Figure S31 and S39, respectively). The binding energy of the new photoemission line, 400-402 eV (Figure S31, S39), corresponded to the N1s photoelectron from reduced nitrogen species undergoing adsorption to LAS (399-401 eV) or BAS ( $NH_4$ <sup>+</sup>, >401 eV). For  $Cu_3(HITP)_2$  and  $Ni_3(HITP)_2$ , adsorption of  $NH_3$  was more difficult to determine due to the overlap of photoemission lines from framework nitrogen and any potential  $NH_3$  (Figure S28, S35).

The effect of NH<sub>3</sub> binding to the frameworks was then assessed for differences in the composition and oxidation state of components. All MOFs in this study exhibited a decreased abundance of surface O species (**Figure S21-S24**) after exposure to NH<sub>3</sub>. This could result from desorbing water, which correlates well with the observations made by DRIFTS of dehydrative adsorption of NH<sub>3</sub> to surface sites observed for all the MOFs (**Table 1**).

Shifts in oxidation states upon analyte binding observed by XPS. The quantification of metal oxidation states by direct observation of the M  $2p_{3/2}$  region was assessed after exposure of the MOFs to NH<sub>3</sub>. Shifts were observed in the oxidation state of Cu in Cu<sub>3</sub>(HITP)<sub>2</sub> and Cu<sub>3</sub>(HHTP)<sub>2</sub>. The percentage of Cu in the Cu<sup>II</sup> oxidation state in Cu<sub>3</sub>(HITP)<sub>2</sub> decreased by  $6\pm1\%$ . In Cu<sub>3</sub>(HHTP)<sub>2</sub> an increase in Cu<sup>II</sup> by  $10\pm2\%$  was observed (**Figure S25-S26**).

The observed metal oxidation state shifts for Cu-containing MOFs were hypothesized to be countered by the opposite redox reaction at the ligands. We, therefore, anticipated oxidation of ligands in  $Cu_3(HITP)_2$  upon exposure to

 $NH_3$  and reduction of ligands in  $Cu_3(HHTP)_2$  in response to  $NH_3$  exposure. The oxidation state of ligands, which corresponded to the average charge per ligand, was calculated for each MOF in the pristine state and after exposure to  $NH_3$ . The counter charge per ligand (charge/ligand) was calculated by determining the ratio of reduced to oxidized heteroatom species (C=X:C-X, where X= 0, N, **Supporting Information Section-XII, Method II**). The oxidation state populations of Cu and Ni in each framework was then compared to the theoretical counter charge carried by each ligand. This approach was used to confirm that frameworks were charge neutral before and after exposure to  $NH_3$  and that charge transfer redox events were occurring between metal and ligand components upon exposure to  $NH_3$  (**Table 2**)

Both Cu-based MOFs were characterized to be charge neutral frameworks due to the low error between direct observation of Cu2p<sub>3/2</sub> oxidation states and those observed from charge/ligand observations in the heteroatom regions (Table 2). Changes to metal and ligand oxidation states for Cu-containing MOFs confirmed that oxidation or reduction observed in the Cu2p<sub>3/2</sub> region was accompanied by a corresponding opposite redox shift at the ligand. This result indicated that the metal and ligand components were redox partners and shifted redox balance in response to NH<sub>3</sub> binding. By comparison, Ni-based MOFs demonstrated no redox shift upon exposure to NH<sub>3</sub>(Table 2). Charge/ligand analysis showed that Ni<sub>3</sub>(HITP)<sub>2</sub> was charge neutral as a framework. However, a similar analysis for Ni<sub>3</sub>(HHTP)<sub>2</sub> showed a notable mismatch between the magnitude of charge balancing of the organic ligands and the most probable oxidation state of Ni<sup>II</sup> (Table 2). The disagreement between components suggests the presence of stoichiometric charge-balancing counter ions (anions, Figure S40). This type of assessment agreed with the hypothetical structure of Ni<sub>3</sub>(HHTP)<sub>2</sub>, which has been hypothesized to contain structural counter anions in the unit cell of the form OH<sub>x</sub>n<sup>-</sup>.<sup>21</sup>

Each MOF was synthesized three times, and each batch was subject to XPS experimentation (Figure S21-S24) to ensure batch-to-batch reproducibility of relative distributions of redox-active species within the MOF materials. While we were able to achieve batch-to-batch reproducibility in the 1-3% range (Figure S21-S24), the quantitative accuracy of XPS is typically limited to an absolute accuracy of about 10%, due to systematic errors, for example in estimating inelastic mean free paths and baseline subtraction.<sup>72</sup> Therefore, it was imperative to this study that while the precision we obtained allowed comparisons to be made, the accuracy of the XPS experiments was supported by other methods. First, the XPS results concerning the oxidation state of Cu were internally consistent across multiple XPS methods (Table 2). Second, the oxidation state distributions obtained by XPS were corroborated by quantitative EPR (Table 2). Finally, our key observations focused on relative changes in patterns before and after exposure to gases, rather than overall quantification of surface species. This focus on relative comparisons, rather than absolute quantification, allowed confidence in the values obtained for oxidation state distributions for observable species.

Characterization of MOFs by EPR. EPR spectroscopy of the pristine material  $Cu_3(HITP)_2$  revealed a broad

symmetric line shape with a g-value of 2.083. The g-value > 2 indicated the unpaired electron resided primarily in a metal-centered orbital of  $Cu^{II}$  having a spin state of S=1/2. Quantification of the radical concentration (**Supporting Information: Section XIV**) suggested that the pristine material existed as a mixture of Cu valences, only  $36\pm4\%$  of all Cu centers existed as EPR-active  $Cu^{II}$  (**Table 2, Figure S42**). The line shape of the EPR signal did not change after exposure of  $Cu_3(HITP)_2$  to  $NH_3$ . However, the percentage of  $Cu^{II}$  decreased from  $36\pm4\%$  to  $33\pm4\%$ . (**Table 2, Figure 6A**). The small decrease in  $Cu^{II}$  was generally consistent with XPS analysis of Cu oxidation state.

EPR spectroscopy of pristine  $Cu_3(HHTP)_2$  material revealed a broad absorbance band centered at  $g=2.105.^{25}$  The g-value >2 indicated the unpaired electron resided primarily in a metal-centered orbital of  $Cu^{II}$  (**Figure 6**). With exposure to  $NH_3$ , a new line shape included  $g_\perp$  at 2.202 which indicated that the ligand field became more anisotropic with exposure to  $NH_3$ . A concomitant increase in the intensity of the resonant absorbance was observed with exposure to  $NH_3$ . Quantification of the radical concentration

**Table 2.** Quantification of oxidation states of metal node and organic linker components of the MOFs by three distinct XPS methods and one EPR method. XPS method-I was applicable to the MOFs utilizing Cu as the metal node. Method I was based on XPS oxidation state of Cu<sup>II</sup> (for Cu node MOFS). Method II was based on XPS ligand charges from O/N 1s BE shift intensities. Method III was based on EPR analysis. Values indicate the percentage of the Cu within the framework calculated to be in the 2+ oxidation state. (± indicates standard deviation from the mean based on measurements for three syntheses of each MOF)

MOF(+analyte)	Method I: Cu <sup>II</sup> Cu2p <sub>3/2</sub>	Method II: charge/HXTP	Method III: Cu <sup>II</sup> : S=1/2
Cu <sub>3</sub> (HITP) <sub>2</sub>	58±1%	61%	36±4%
$Cu_3(HITP)_2+NH_3$	51±1%	52%	33±4%
$Cu_3(HHTP)_2$	85±1%	79%	82±1%
$Cu_3(HHTP)_2+NH_3$	95±3%	92%	94±2%
Ni <sub>3</sub> (HITP) <sub>2</sub>	theory: Ni <sup>II</sup>	charge/Ni: 1.90	not observed
Ni <sub>3</sub> (HITP) <sub>2</sub> +NH <sub>3</sub>	theory: Ni <sup>II</sup>	charge/Ni: 1.96	not observed
$Ni_3(HHTP)_2$	theory: Ni <sup>II</sup>	charge/Ni: 0.85	not observed
Ni <sub>3</sub> (HHTP) <sub>2</sub> +NH <sub>3</sub>	theory: Ni <sup>II</sup>	charge/Ni: 0.82	not observed

suggested that in the pristine material, 82% of Cu centers existed as EPR-active Cu<sup>II</sup>. Upon exposure to NH<sub>3</sub>, the percentage of Cu<sup>II</sup> increased to 94% (**Figure 6**). This increase was consistent with XPS analysis of Cu<sub>3</sub>(HHTP)<sub>2</sub>.

EPR spectroscopy of pristine  $Ni_3(HITP)_2$  material showed a sharp absorbance band at g=1.97 (**Figure 6**). The absorbance band was doubly integrated to reveal that  $7.9 \times 10^{-3}$ % of ligands exhibited excess spin originating from a ligand-centered free radical. The g-value and the intensity of the band at g=1.97 band did not change upon exposure to  $NH_3$  (**Figure 6**).

EPR analysis of  $Ni_3(HHTP)_2$  showed no absorbance across the observed range (**Figure 6**), consistent with the presence of  $Ni^{II}$  and absence of uncoupled ligand-centered free radicals. Exposure of the MOF to  $NH_3$  produced no observable changes in the EPR spectra.

Analyte-induced spin density changes observed by EPR. EPR spectroscopy was able to reveal three important insights when comparing the pristine MOFs against their NH<sub>3</sub>-exposed counterparts. *First*, Cu-based MOFs exhibited walency in the pristine state for both Cu<sub>3</sub>(HITP)<sub>2</sub> (36±4% Cu<sup>II</sup>: 64±4% Cu<sup>I</sup>) and Cu<sub>3</sub>(HHTP)<sub>2</sub> (82±1 Cu<sup>II</sup>: 18±1 Cu<sup>I</sup>). NH<sub>3</sub> induced a slight reduction of Cu in Cu<sub>3</sub>(HITP)<sub>2</sub> (-3±2% Cu<sup>II</sup>) and a significant shift in the oxidation of Cu in Cu<sub>3</sub>(HHTP)<sub>2</sub> (+13±3% Cu<sup>II</sup>). *Second*, analysis of the line shape in Cu<sub>3</sub>(HITP)<sub>2</sub> exposure experiments suggested that the ligand field surrounding Cu<sup>II</sup> centers was isotropic in the pristine state and after exposure to NH<sub>3</sub>. Similar analysis of line shape in Cu<sub>3</sub>(HHTP)<sub>2</sub> revealed that the isotropic line shape of the pristine sample changed indicating a change in the coordination sphere around the EPR active center. The

distinct responses of both materials suggested that the EPR-active  $Cu^{II}$  centers in  $Cu_3(HHTP)_2$  experienced strong interactions with  $NH_3$  while those in  $Cu_3(HITP)_2$  did not. *Third*, the Ni-based analogues exhibited weak or no EPR signal. Radical density in  $Ni_3(HITP)_2$  was substoichiometric, suggesting that detected radicals may be localized at defect sites or terminal edges of the framework, rather than a systematic part of the  $Ni_3(HITP)_2$  unit cell. No radical character was detected in  $Ni_3(HHTP)_2$ , suggesting either the absence of radical functionality or antiferromagnetic coupling of radical species. No significant change in spin content or spin density was observed for  $Ni_3(HITP)_2$  and  $Ni_3(HHTP)_2$  MOFs upon exposure to  $NH_3$  (Figure 6).

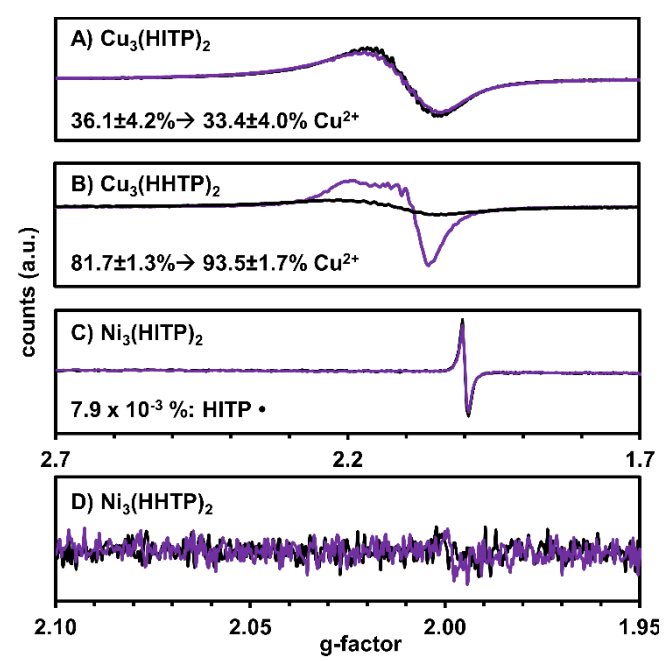


**Figure 6**: EPR spectroscopy provided a quantitative understanding of the total populations of metal oxidation states within the bulk as well as the surface. The first derivative of the absorbance spectra for each MOF is plotted for the pristine material (black trace) and after exposure to NH<sub>3</sub> (purple trace).

Structural characterization of MOFs after gas exposure by PXRD analysis. While significant changes in oxidation state were observed spectroscopically, the structure of the MOFs remained intact, as confirmed by PXRD (Figure S45-S48). The HITP-based MOFs showed no observable change in crystal phase and no change to their powder pattern upon exposure to NH<sub>3</sub>, Pyr, CD<sub>3</sub>CN (Figure S46-S47). The HHTP-based MOFs showed no change in crystal phase upon exposure to the same gases (Figure S45, S48). However, both Ni<sub>3</sub>(HHTP)<sub>2</sub> and Cu<sub>3</sub>(HHTP)<sub>2</sub> showed a shift of the diffraction peak corresponding to the interlayer stacking distance (Cu<sub>3</sub>(HHTP)<sub>2</sub>: [002], Ni<sub>3</sub>(HHTP)<sub>2</sub>: [004]) to lower 2θ values (**Figure S45, S48**). This shift indicated that the adsorption of NH3, Pyr, and CD3CN in the case of Ni<sub>3</sub>(HHTP)<sub>2</sub>, and NH<sub>3</sub> in the case of Cu<sub>3</sub>(HHTP)<sub>2</sub> caused a small increase in the interlayer stacking distance. Using Bragg's law, the increase in interlayer distance was computed to be 0.014 Å for  $Cu_3(HHTP)_2$  upon adsorption of  $NH_3$ . The increase of the interlayer stacking distance was consistent with the observations by Rubio-Gimenez et al. in Cu<sub>3</sub>(HHTP)<sub>2</sub> thin films exposed to NH<sub>3</sub>.<sup>20</sup> We did not use additional heating or vacuum activation procedures before exposing the MOFs to NH<sub>3</sub>. The magnitude of the peak shift we observe was comparable to the peak shift previously reported.20

Bottom-up control over surface chemistry, redox activity, and host-guest interactions in HXTP-based conductive MOFs. The application of four distinct and overlying spectroscopic techniques including DRIFTS, EPR, XPS, and PXRD with several basic probe gases was able to discern the dominant type of surface acidity for each MOF as well as redox shifts involving MOF components consequent to gas binding, while confirming that all MOFs remained structurally intact after exposure. The selection of

techniques allowed a detailed investigation of structural changes by PXRD, surface chemistry by XPS, while also allowing for characterization of interactions under conditions relevant to chemical sensing using DRIFTS and EPR. Three major findings were revealed using the four complimentary spectroscopic methods.

First, DRIFTS studies determined that the mode of interaction between basic gases and the surface of the MOFs was tunable and determined primarily by the nature of the organic ligand, and secondarily by the nature of the metal center used in synthesis of the four MOFs studied. Our selection of probes (NH<sub>3</sub>, CD<sub>3</sub>CN, Pyr) determined that Cu<sub>3</sub>(HITP)<sub>2</sub> and Ni<sub>3</sub>(HITP)<sub>2</sub> were dominated by weak LAS, while Cu<sub>3</sub>(HHTP)<sub>2</sub> and Ni<sub>3</sub>(HHTP)<sub>2</sub> were dominated by strong LAS and strong BAS (**Figure 7A**).

The second major finding of this work was that NH<sub>3</sub> induced a shift in oxidation state of Cu in Cu<sub>3</sub>(HITP)<sub>2</sub> and Cu<sub>3</sub>(HHTP)<sub>2</sub> (**Figure 7B**). This finding was consistently revealed by XPS and EPR. The shift observed by XPS was moderate for Cu<sub>3</sub>(HHTP)<sub>2</sub> (a shift of +10±2% towards Cu<sup>II</sup>) and opposite (-9±4% towards Cu<sup>II</sup>) for Cu<sub>3</sub>(HITP)<sub>2</sub>. EPR confirmed a significant shift observed for Cu<sub>3</sub>(HHTP)<sub>2</sub> (+12±3% towards Cu<sup>II</sup>) The resulting distribution of oxidation states of Cu<sup>II</sup> by these two methods were in good agreement (EPR: 94±2%, XPS:95±3%). To rationalize this shift in oxidation state in Cu<sub>3</sub>(HHTP)<sub>2</sub>, we propose a mechanism where the reduction potential of the Cu centers decreases when NH<sub>3</sub> is adsorbed (Figure 7B). In this scenario the electrons liberated by the oxidized copper would be shuttled to non-innocent dioxolene linkers maintaining charge balance within the neutral framework. Using XPS we confirmed that the Cubased frameworks were charge-neutral before and after NH<sub>3</sub> exposure and the ligand components of Cu<sub>3</sub>(HHTP)<sub>2</sub> were reduced in response to NH<sub>3</sub>. The oxidation state shifts observed for Cu<sub>3</sub>(HITP)<sub>2</sub> were small, but internally consistent between magnitude of reduction of Cu-components (-6% Cu<sup>II</sup>) and oxidation of ligand components. This evidence suggests that the redox balance between ligand and metal readily underwent rearrangement upon adsorption of basic gases.

Third, the two examples of Ni-based systems showed surface chemistries of LAS (Ni<sub>3</sub>(HITP)<sub>2</sub>) or BAS and LAS (Ni<sub>3</sub>(HHTP)<sub>2</sub>) by DRIFTS. Despite having amenable surface acidities, neither system exhibited strong ring perturbations by DRIFTS after exposure to NH<sub>3</sub> and CD<sub>3</sub>CN, compared to the Cu-containing analogues. Similarly, no oxidation or reduction of Ni<sup>II</sup> centers in response to NH<sub>3</sub> was observed by either EPR or XPS (**Figure 6**). This observation provided further evidence for the importance of the Cu metal center in providing redox capabilities in response to gas binding.

The experiments performed in this body of work have determined that MOFs containing redox active metals (Cu) and ligands are more electronically responsive to the presence of basic gases, such as NH<sub>3</sub>, when compared to MOFs that only contain redox active ligands (Ni<sub>3</sub>(HHTP)<sub>2</sub>, Ni<sub>3</sub>(HITP)<sub>2</sub>). This trend is reflected in the reactivity observed as part of chemiresistive studies performed by us and others.<sup>11-14, 20, 23</sup> Consensus among published reports indicates that Cu is superior to Ni for construction of MOFs that exhibit operative changes in resistance when exposed

to NH<sub>3</sub> gas. 11-14, 20, 23 Specifically, previous studies have found that Cu<sub>3</sub>(HHTP)<sub>2</sub> and Cu<sub>3</sub>(HITP)<sub>2</sub> exhibit a partially reversible increase in resistance upon exposure to NH3 while Ni<sub>3</sub>(HHTP)<sub>2</sub> and Ni<sub>3</sub>(HITP)<sub>2</sub> exhibit minimal change or no change in resistance in response to similar conditions. 11-14, <sup>20, 23</sup> This work indicates that the Cu-containing MOF analogues exhibit observable redox shifts among framework components, perturbations to the BEA, and partially reversible binding of NH<sub>3</sub>, while Ni-based MOFs exhibit minimal observable redox activity among framework components when exposed to NH<sub>3</sub>. This general observation is also consistent with our previous report of voltammetric characterization of redox activity of this class of framework materials deposited on the surface of glassy carbon electrodes, which revealed strong voltage-driven redox processes for Cu-based MOFs, and absence of such processes for Ni-based MOFs.73

Our studies using PXRD and DRIFTS also provide the conclusion that when  $\text{NH}_3$  displaces water to adsorb at Lewis acid sites, the binding is strong and irreversible, and does not lead to a structural changes  $(\text{Ni}_3(\text{HITP})_2, \text{Cu}_3(\text{HITP})_2)$ . Alternatively, when it coordinates to BAS, it is more reversibly bound, and it induces structural changes in the aromatic ring system  $(\text{Cu}_3(\text{HITP})_2, \text{Ni}_3(\text{HITP})_2)$ . The resulting structural changes manifest as small increases in the interlayer stacking distance. The increased stacking distance was consistent with a decrease in the BEA for HHTP-based MOFs and a decrease in the conductivity observed by us an others in response to  $\text{NH}_3.^{3,13,20}$ 

Direct comparisons cannot be made between previous studies and this work for two main reasons. *First* higher concentrations of analytes, necessary for spectroscopic analysis, were used in this study while sensing experiments typically use low ppm concentrations. *Second*, chemiresistive sensing experiments are performed under an applied potential, which may alter the balance of redox states from what we observe in this work.

Despite these limitations, certain interpretations relevant to the transduction mechanism of chemiresistive sensing can be inferred from the results we have obtained. *First*, redox activity of the metal is an important feature of 2D MOFs designed for chemiresistive sensing. *Second*, that the partial reversibility observed in the chemiresistive response of Cu<sub>3</sub>(HHTP)<sub>2</sub> to NH<sub>3</sub> could be due to the presence of combined weak Brønsted acidity and Lewis acidity observed on Cu<sub>3</sub>(HHTP)<sub>2</sub> by spectroscopic methods. *Third*, the reversible decrease in the BEA of Cu<sub>3</sub>(HHTP)<sub>2</sub>+NH<sub>3</sub> correlates with the conductivity decrease observed in chemiresistive sensing of NH<sub>3</sub>.<sup>3</sup>, <sup>13</sup>, <sup>20</sup> Similarly, the reversible increase in the BEA observed for Cu<sub>3</sub>(HITP)<sub>2</sub>+NH<sub>3</sub> correlates well with the conductivity increase observed chemiresistively.<sup>14</sup>

### **CONCLUSIONS**

This paper provides the first explicit identification of specific interactions between basic gases and surface host sites for a series of 2D conductive MOFs. Using a series of four structurally similar MOFs, we have shown that surface chemistry in this class of materials can emerge through self-assembly. Across the four MOF structures compared herein, the identity of the metal center (Cu, Ni) and the identity of ligand (HITP, HHTP) contribute significantly towards the

surface chemistry and the response of embedded host-sites toward basic probe gases (NH<sub>3</sub>, CD<sub>3</sub>CN, Pyr). We identified the organic ligand as the primary determinant of acidity (LAS, BAS), while the metal center was the primary determinant of redox activity in response to binding NH<sub>3</sub>. Through four complementary spectroscopic methods, we showed that the electronic structure of these MOFs is modulated on the molecular scale by the presence of the analyte probe, while preserving the structural fidelity of these materials. The enhanced redox activity of the Cu-based MOFs compared to their Ni-analogues demonstrated that metal centers, when paired with non-innocent ligands, could impart stimuli-responsive functionality to a bulk framework. Although results do not explicitly identify the individual contributions of edge site, basal plane, and pore volume to the overall observed surface chemistry, PXRD results and similarity of the XPS and EPR estimates of the oxidation state shifts indicate that NH<sub>3</sub> is bound through the pore volume, in a manner consistent with the model proposed by Rubio-Gimenez et al. Our work furthers their proposed mechanism of chemiresistive sensing by highlighting the importance of BAS in the structural changes observed by PXRD. The correlations we observe between baseline BEA, chemiresistive sensing, structural changes, and redox shifts, indicate a complex sensing mechanism where structural and compositional factors directly and indirectly influence the ability of these materials to transduce adsorption of basic gases.

As the structures of stacked 2D materials are highly anisotropic, we anticipate that identifying the chemistry on distinct surfaces will provide insightful information into the structure–property relationships of these morphologically diverse materials. Further investigation of the reactivity of specific crystalline facets through spectroscopic and computational methods has the potential to provide insight into how facet-specific surface chemistry dominates function within this class of crystalline materials.

# A) structure–property trends for M<sub>3</sub>(HXTP)<sub>2</sub> MOFs H X H N, Cu, N H X' H Weak acidity weak acidity x, x' = CUS, OH<sub>x</sub> B) redox equilibrium shifted by gas binding

## i. gas X=NH



**Figure 7. A)** Summary of general trends in acidity and redox activity of MOFs probed by basic gases. **B)** Proposed mechanism for the shift of oxidation states observed for Cucontaining species upon binding of a basic gas. B: - basic gas, M - metal center, X - ligand heteroatom, L - ligand ( $H_2O$  at edge sites, heteroatom from HXTP at basal plane sites).

Recent reports by Long<sup>74</sup> and Marti-Gastaldo<sup>24</sup> describe chemiresistive behavior from a mechanistic perspective for MOFs composed of metal bis(dithiolene) and metal bis(dioxolene) linkages, respectively. The report by Long and coworkers identified the degree of solvation to be highly important in the conductivity of MOFs that perform chemical sensing using physisorption-based chemiresistivity.  $^{74}$  Work by Marti-Gastaldo and coworkers investigated NH<sub>3</sub> binding to Cu<sub>3</sub>(HHTP)<sub>2</sub> sheets.<sup>24</sup>. As noted by Long and coworkers, an important line of inquiry focuses on the behavior of redox active frameworks and adsorbates.74 Our contribution offers an important step towards this goal by investigating the stimuli-responsive redox state of components within the framework and how components ultimately control surface chemistry. The findings presented in this report are valuable for understanding the complexity of sensing capabilities across this family of materials, 1, 13, 15, 23, 75 and for design of future chemiresistive systems.

This contribution clarifies and highlights the role of bottom-up differentiation of surface acidity and redox activity of 2D conductive materials. Our studies established that the previously observed differential chemiresistive response of this class of MOFs stems from the dual interplay between surface acidity and redox activity. We anticipate that this report will provide a foundation for the continued exploration of redox activity and adsorbate-modulated redox activity in this class of materials. Ultimately, this work provides a necessary and useful tool to allow the development of these materials towards targeted applications.

### ASSOCIATED CONTENT

**Supporting Information** The supporting information is available free of charge on the ACS Publications website at DOI: xx.xxxxxxx

Experimental methods, characterization of MOF structure by SEM and PXRD, surface characterization by DRIFTS and XPS, and spin-density characterization by EPR

### **AUTHOR INFORMATION**

### **Corresponding Authors**

\*(K.A.M.) katherine.a.mirica@dartmouth.edu \*(B.G.F.) briangf@maine.edu

### ORCID

Robert M. Stolz: 0000-0002-9291-0794 Akbar Mahdavi-Shakib: 0000-0003-1763-6761 Brian G. Frederick: 0000-0002-5715-6511 Katherine A. Mirica: 0000-0002-1779-7568

### Notes

The authors declare no competing financial interest.

### **ACKNOWLEDGMENT**

K.A.M. acknowledges support from startup funds provided by Dartmouth College, from the Walter and Constance Burke Research Initiation Award, Army Research Office Young Investigator Program Grant No. W911NF-17-1-0398, National Science Foundation EPSCoR award (#1757371), Sloan Research Fellowship (FG-2018-10561), 3M Non-Tenured Faculty Award, the Cottrell Scholar Award (#26019) from the Research Corporation for Science Advancement, and the NSF CAREER Award (#1945219). The authors thank the University Instrumentation Center at the University of New Hampshire (Durham, NH) for the access to XPS, Mr. Maciej M. Kmiec for assistance with EPR, and Charles Daghlian for his help with SEM.

### **REFERENCES**

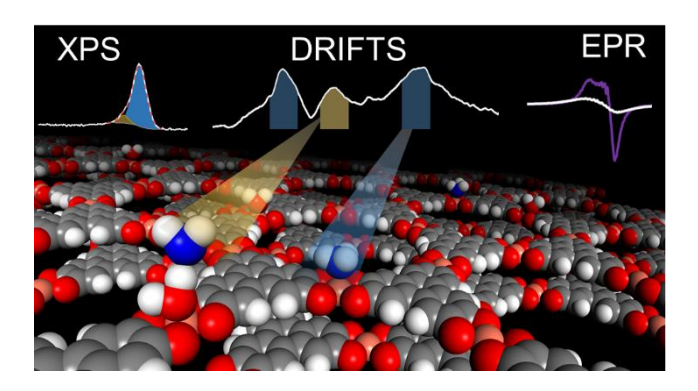
- 1. Ko, M.; Mendecki, L.; Mirica, K. A., Conductive Two-Dimensional Metal-Organic Frameworks as Multifunctional Materials. *Chen. Commun.* **2018**, *54* (57), 7873-7891.
- 2. Sun, L.; Campbell, M. G.; Dinca, M., Electrically Conductive Porous Metal-Organic Frameworks. *Angew. Chem. Int. Ed. Engl.* **2016**, *55* (11), 3566-3579.
- 3. Yao, M. S.; Lv, X. J.; Fu, Z. H.; Li, W. H.; Deng, W. H.; Wu, G. D.; Xu, G., Layer-by-Layer Assembled Conductive Metal-Organic Framework Nanofilms for Room-Temperature Chemiresistive Sensing. *Angew. Chem. Int. Ed. Engl.* **2017**, *56* (52), 16510-16514.
- 4. Mendecki, L.; Ko, M.; Zhang, X.; Meng, Z.; Mirica, K. A., Porous Scaffolds for Electrochemically Controlled Reversible Capture and Release of Ethylene. *J. Am. Chem. Soc.* **2017**, *139* (48), 17229-17232.
- 5. Sheberla, D.; Bachman, J. C.; Elias, J. S.; Sun, C.-J.; Shao-Horn, Y.; Dincă, M., Conductive MOF Electrodes for Stable Supercapacitors with High Areal Capacitance. *Nat. Mater* **2016**, *16* (2), 220-224.
- 6. Wu, G.; Huang, J.; Zang, Y.; He, J.; Xu, G., Porous Field-Effect Transistors Based on a Semiconductive Metal–Organic Framework. *J. Am. Chem. Soc.* **2017**, *139* (4), 1360-1363.
- 7. Sheberla, D.; Sun, L.; Blood-Forsythe, M. A.; Er, S.; Wade, C. R.; Brozek, C. K.; Aspuru-Guzik, A.; Dinca, M., High Electrical Conductivity in Ni(3)(2,3,6,7,10,11-hexaiminotriphenylene)(2), a Semiconducting Metal-Organic Graphene Analogue. *J. Am. Chem. Soc.* **2014**, *136* (25), 8859-8862.
- 8. Clough, A. J.; Yoo, J. W.; Mecklenburg, M. H.; Marinescu, S. C., Two-Dimensional Metal-Organic Surfaces for Efficient Hydrogen Evolution from Water. *J. Am. Chem. Soc.* **2015**, *137* (1), 118-121.

- 9. Mendecki, L.; Mirica, K. A., Conductive Metal–Organic Frameworks as Ion-to-Electron Transducers in Potentiometric Sensors. *ACS Appl. Mater. Interfaces* **2018**, *10* (22), 19248-19257.
- 10. Sun, L.; Campbell, M. G.; Dincă, M., Electrically Conductive Porous Metal-Organic Frameworks. *Angew. Chem. Int. Ed.* **2016**, *55* (11), 3566-3579.
- 11. Yao, M.-S.; Lv, X.-J.; Fu, Z.-H.; Li, W.-H.; Deng, W.-H.; Wu, G.-D.; Xu, G., Layer-by-Layer Assembled Conductive Metal-Organic Framework Nanofilms for Room-Temperature Chemiresistive Sensing. *Angew. Chem.* **2017**, *129* (52), 16737-16741.
- 12. Smith, M. K.; Mirica, K. A., Self-Organized Frameworks on Textiles (SOFT): Conductive Fabrics for Simultaneous Sensing, Capture, and Filtration of Gases. *J. Am. Chem. Soc.* **2017**, *139* (46), 16759-16767.
- 13. Ko, M.; Aykanat, A.; Smith, M. K.; Mirica, K. A., Drawing Sensors with Ball-Milled Blends of Metal-Organic Frameworks and Graphite. *Sensors (Basel)* **2017**, *17* (10).
- 14. Campbell, M. G.; Sheberla, D.; Liu, S. F.; Swager, T. M.; Dinca, M., Cu(3)(hexaiminotriphenylene)(2): An Electrically Conductive 2D Metal-Organic Framework for Chemiresistive Sensing. *Angew. Chem. Int. Ed. Engl.* **2015**, *54* (14), 4349-4352.
- 15. Campbell, M. G.; Liu, S. F.; Swager, T. M.; Dinca, M., Chemiresistive Sensor Arrays from Conductive 2D Metal-Organic Frameworks. J. Am. Chem. Soc. 2015, 137 (43), 13780-13783.
- 16. Park, J.; Hinckley, A. C.; Huang, Z.; Feng, D.; Yakovenko, A. A.; Lee, M.; Chen, S.; Zou, X.; Bao, Z., Synthetic Routes for a 2D Semiconductive Copper Hexahydroxybenzene Metal-Organic Framework. J. Am. Chem. Soc. 2018, 140 (44), 14533-14537.
- 17. Park, J.; Lee, M.; Feng, D.; Huang, Z.; Hinckley, A. C.; Yakovenko, A.; Zou, X.; Cui, Y.; Bao, Z., Stabilization of Hexaaminobenzene in a 2D Conductive Metal–Organic Framework for High Power Sodium Storage. *J. Am. Chem. Soc.* **2018**, *140* (32), 10315-10323.
- 18. Duhović, S.; Dincă, M., Synthesis and Electrical Properties of Covalent–Organic Frameworks with Heavy Chalcogens. *Chem. Mater.* **2015**, *27* (16), 5487-5490.
- 19. Reghu, A.; LeGore, L. J.; Vetelino, J. F.; Lad, R. J.; Frederick, B. G., Distinguishing Bulk Conduction from Band Bending Transduction Mechanisms in Chemiresistive Metal Oxide Gas Sensors. *J. Phys. Chem. C* **2018**, *122* (19), 10607-10620.
- 20. Rubio-Gimenez, V.; Almora-Barrios, N.; Escorcia-Ariza, G.; Galbiati, M.; Sessolo, M.; Tatay, S.; Marti-Gastaldo, C., Origin of the Chemiresistive Response of Ultrathin Films of Conductive Metal-Organic Frameworks. *Angew. Chem. Int. Ed. Engl.* **2018**, *57* (46), 15086-15090.
- 21. Hmadeh, M.; Lu, Z.; Liu, Z.; Gándara, F.; Furukawa, H.; Wan, S.; Augustyn, V.; Chang, R.; Liao, L.; Zhou, F.; Perre, E.; Ozolins, V.; Suenaga, K.; Duan, X.; Dunn, B.; Yamamto, Y.; Terasaki, O.; Yaghi, O. M., New Porous Crystals of Extended Metal–Catecholates. *Chem. Mater.* **2012**, *24* (18), 3511-3513.
- 22. Day, R. W.; Bediako, D. K.; Rezaee, M.; Parent, L. R.; Skorupskii, G.; Arguilla, M. Q.; Hendon, C. H.; Stassen, I.; Gianneschi, N. C.; Kim, P.; Dinca, M., Single Crystals of Electrically Conductive Two-Dimensional Metal-Organic Frameworks: Structural and Electrical Transport Properties. *ACS Cent Sci* **2019**, *5* (12), 1959-1964.
- 23. Smith, M. K.; Jensen, K. E.; Pivak, P. A.; Mirica, K. A., Direct Self-Assembly of Conductive Nanorods of Metal-Organic Frameworks into Chemiresistive Devices on Shrinkable Polymer Films. *Chem. Mater.* **2016**, *28* (15), 5264-5268.
- 24. Rubio-Gimenez, V.; Galbiati, M.; Castells-Gil, J.; Almora-Barrios, N.; Navarro-Sanchez, J.; Escorcia-Ariza, G.; Mattera, M.; Arnold, T.; Rawle, J.; Tatay, S.; Coronado, E.; Marti-Gastaldo, C., Bottom-Up Fabrication of Semiconductive Metal-Organic Framework Ultrathin Films. *Adv. Mater.* **2018**, *30* (10).
- 25. Yang, L.; He, X.; Dinca, M., Triphenylene-Bridged Trinuclear Complexes of Cu: Models for Spin Interactions in Two-Dimensional Electrically Conductive Metal-Organic Frameworks. *J. Am. Chem. Soc.* **2019**, *141* (26), 10475-10480.
- 26. Ma, J.-P.; Wang, S.-Q.; Zhao, C.-W.; Yu, Y.; Dong, Y.-B., Cu(II)-Metal-Organic Framework with Open Coordination Metal Sites for Low Temperature Thermochemical Water Oxidation. *Chem. Mater.* **2015**, *27* (11), 3805-3808.
- 27. Zhang, X.; Vermeulen, N. A.; Huang, Z.; Cui, Y.; Liu, J.; Krzyaniak, M. D.; Li, Z.; Noh, H.; Wasielewski, M. R.; Delferro, M.; Farha, O. K., Effect of Redox "Non-Innocent" Linker on the Catalytic Activity of

- Copper-Catecholate-Decorated Metal-Organic Frameworks. ACS Appl. Mater. Interfaces 2018, 10 (1), 635-641.
- 28. Huxley, M. T.; Coghlan, C. J.; Bloch, W. M.; Burgun, A.; Doonan, C. J.; Sumby, C. J., X-ray crystallographic insights into post-synthetic metalation products in a metal-organic framework. *Philos Trans A Math Phys Eng Sci* **2017**, *375* (2084).
- 29. Pierpont, C. G.; Buchanan, R. M., Transition Metal Complexes of *o*-Benzoquinone, *o*-Semiquinone, and Catecholate Ligands. *Coord. Chem. Rev.* **1981**, *38* (1), 45-87.
- 30. Jian, L.; Chen, C.; Lan, F.; Deng, S.; Xiao, W.; Zhang, N., Catalytic activity of unsaturated coordinated Cu-MOF to the hydroxylation of phenol. *Solid State Sci.* **2011**, *13* (5), 1127-1131.
- 31. Liu, P.; Redekop, E.; Gao, X.; Liu, W. C.; Olsbye, U.; Somorjai, G. A., Oligomerization of Light Olefins Catalyzed by Bronsted-Acidic Metal-Organic Framework-808. *J. Am. Chem. Soc.* **2019**, *141* (29), 11557-11564.
- 32. Jiang, J.; Yaghi, O. M., Bronsted Acidity in Metal-Organic Frameworks. *Chem. Rev.* **2015**, *115* (14), 6966-6997.
- 33. Mitchell, M. B., Fundamentals and Applications of Diffuse Reflectance Infrared Fourier Transform (DRIFT) Spectroscopy. ACS Publications: Washington, D. C., 1993; Vol. 236, p 351-375.
- 34. de Donato, P.; Cases, J. M.; Humbert, B.; Lutgen, P.; Feyder, G., Analysis of Polymer Films by Diffuse Reflectance FTIR Spectroscopy: Characterization of Terminal Carboxyl Functionalities. *J. Polym. Sci., Part B: Polym. Phys.* **1992**, *30* (12), 1305-1310.
- 35. Zaera, F., New Advances in the Use of Infrared Absorption Spectroscopy for the Characterization of Heterogeneous Catalytic Reactions. *Chem. Soc. Rev.* **2014**, *43* (22), 7624-7663.
- 36. Fuller, M. P.; Griffiths, P. R., Diffuse Reflectance Measurements by Infrared Fourier Transform Spectrometry. *Anal. Chem.* **2002**, *50* (13), 1906-1910.
- 37. Mahdavi-Shakib, A.; Arce-Ramos, J. M.; Austin, R. N.; Schwartz, T. J.; Grabow, L. C.; Frederick, B. G., Frequencies and Thermal Stability of Isolated Surface Hydroxyls on Pyrogenic TiO<sub>2</sub> Nanoparticles. *J. Phys. Chem. C* **2019**, *123* (40), 24533-24548.
- 38. Mahdavi-Shakib, A.; Husremovic, S.; Ki, S.; Glynn, J.; Babb, L.; Sempel, J.; Stavrinoudis, I.; Arce-Ramos, J.-M.; Nelson, R.; Grabow, L. C.; Schwartz, T. J.; Frederick, B. G.; Austin, R. N., Titania Surface Chemistry and Its Influence on Supported Metal Catalysts. *Polyhedron* **2019**, *170*, 41-50.
- 39. Kim, C. S.; Lad, R. J.; Tripp, C. P., Interaction of Organophosphorous Compounds with  $TiO_2$  and  $WO_3$  Surfaces Probed by Vibrational Spectroscopy. *Sensors and Actuators B: Chemical* **2001**, 76 (1-3), 442-448.
- 40. Panayotov, D. A.; Burrows, S. P.; Morris, J. R., Infrared Spectroscopic Studies of Conduction Band and Trapped Electrons in UV-Photoexcited, H-Atom n-Doped, and Thermally Reduced TiO<sub>2</sub>. *J. Phys. Chem. C* **2012**, *116* (7), 4535-4544.
- 41. Nijdam, A. J.; Cheng, M. M.-C.; Ferrari, M., X-Ray Photoelectron Spectroscopy Depth Profile of Chemically Modified Porous Silicon. *J. Vac. Sci. Technol.* **2006**, *24* (2), 852-854.
- 42. Roessler, M. M.; Salvadori, E., Principles and Applications of EPR Spectroscopy in the Chemical Sciences. *Chem. Soc. Rev.* **2018**, *47* (8), 2534-2553.
- 43. Chiesa, M.; Giamello, E.; Che, M., EPR Characterization and Reactivity of Surface-Localized Inorganic Radicals and Radical Ions. *Chem. Rev.* **2010**, *110* (3), 1320-1347.
- 44. Holder, C. F.; Schaak, R. E., Tutorial on Powder X-ray Diffraction for Characterizing Nanoscale Materials. *ACS Nano* **2019**, *13* (7), 7359-7365.
- 45. Snyder, R. J. R. L., Introduction to X-ray powder diffractometry. Wiley: New York, 1996; Vol. xxii.
- 46. Cullity, B. D., *Elements of X-Ray Diffraction*. Addison-Wesley Publishing Company, Inc.: Reading, MA, 1956.
- 47. Herbstein, F. H., How precise are measurements of unit-cell dimensions from single crystals? *Acta Crystallogr B* **2000**, *56* (Pt 4), 547-557.
- 48. Tsyganenko, A. A.; Pozdnyakov, D. V.; Filimonov, V. N., Infrared Study of Surface Species Arising from Ammonia Adsorption on Oxide Surfaces. *J. Mol. Struct.* **1975**, *29* (2), 299-318.
- 49. Amores, J. G.; Escribano, V. S.; Ramis, G.; Busca, G., An FT-IR Study of Ammonia Adsorption and Oxidation Over Anatase-Supported Metal Oxides. *Appl. Catal. B* **1997**, *13* (1), 45-58.

- 50. Barzetti, T.; Selli, E.; Moscotti, D.; Forni, L., Pyridine and Ammonia as Probes for FTIR Analysis of Solid Acid Catalysts. *J. Chem. Soc., Faraday Trans.* **1996**, *92* (8), 1401-1407.
- 51. Morterra, C.; Peñarroya Mentruit, M.; Cerrato, G., Acetonitrile Adsorption as an IR Spectroscopic Probe for Surface Acidity/Basicity of Pure and Modified Zirconias. *Phys. Chem. Chem. Phys.* **2002**, *4* (4), 676-687.
- 52. Otero Areán, C.; Escalona Platero, E.; Peñarroya Mentruit, M.; Rodríguez Delgado, M.; Llabrés i Xamena, F. X.; García-Raso, A.; Morterra, C., The Combined Use of Acetonitrile and Adamantane–Carbonitrile as IR Spectroscopic Probes to Discriminate Between External and Internal Surfaces of Medium Pore Zeolites. *Microporous Mesoporous Mater.* **2000**, *34* (1), 55-60.
- 53. Williams, D. E., Semiconducting oxides as gas-sensitive resistors. *Sensors and Actuators B: Chemical* **1999**, *57* (1-3), 1-16.
- 54. Szaleniec, M.; Drzewiecka-Matuszek, A.; Witko, M.; Hejduk, P., Ammonium Adsorption on Brønsted Acidic Centers on Low-Index Vanadium Pentoxide Surfaces. *J. Mol. Model.* **2013**, *19* (10), 4487-4501.
- 55. Suganuma, S.; Murakami, Y.; Ohyama, J.; Torikai, T.; Okumura, K.; Katada, N., Assignments of Bending Vibrations of Ammonia Adsorbed on Surfaces of Metal Oxides. *Catal. Lett.* **2015**, *145* (10), 1904-1912.
- 56. Chen, P.; Schonebaum, S.; Simons, T.; Rauch, D.; Dietrich, M.; Moos, R.; Simon, U., Correlating the Integral Sensing Properties of Zeolites with Molecular Processes by Combining Broadband Impedance and DRIFT Spectroscopy—A New Approach for Bridging the Scales. *Sensors (Basel)* **2015**, *15* (11), 28915-28941.
- 57. Lercher, J. A.; Gründling, C.; Eder-Mirth, G., Infrared Studies of the Surface Acidity of Oxides and Zeolites Using Adsorbed Probe Molecules. *Catal. Today* **1996**, *27* (3-4), 353-376.
- 58. Nguyen, N. T.; Furukawa, H.; Gandara, F.; Trickett, C. A.; Jeong, H. M.; Cordova, K. E.; Yaghi, O. M., Three-Dimensional Metal-Catecholate Frameworks and Their Ultrahigh Proton Conductivity. *J. Am. Chem. Soc.* **2015**, *137* (49), 15394-15397.
- 59. Bucko, T.; Hafner, J.; Benco, L., Adsorption and Vibrational Spectroscopy of Ammonia at Mordenite: Ab Initio Study. *J. Chem. Phys.* **2004**, *120* (21), 10263-10277.
- 60. Chan, W.-T.; Fournier, R., Binding of Ammonia to Small Copper and Silver Clusters. *Chem. Phys. Lett.* **1999**, *315* (3-4), 257-265.
  61. Daniell, W.; Topsøe, N. Y.; Knözinger, H., An FTIR Study of the Surface Acidity of USY Zeolites: Comparison of CO, CD₃CN, and C₅H₅N Probe Molecules. *Langmuir* **2001**, *17* (20), 6233-6239.
- 62. Pelmenschikov, A. G.; van Santen, R. A.; Janchen, J.; Meijer, E., Acetonitrile-d<sub>3</sub> as a Probe of Lewis and Brønsted Acidity of Zeolites. *J. Phys. Chem.* **1993**, *97* (42), 11071-11074.

- 63. Cataldo, F., A Revision of the Gutmann Donor Numbers of a Series of Phophoramides Including TEPA. Eur. Chem. Bull. 2015, 92-97.
  64. CRC Handbook of Chemistry and Physics: A Ready-Reference Book of Chemical and Physical Data. 90th ed.; CRC Press: Boca Raton, Florida, 2009-2010.
- 65. Litke, A.; Su, Y.; Tranca, I.; Weber, T.; Hensen, E. J. M.; Hofmann, J. P., Role of Adsorbed Water on Charge Carrier Dynamics in Photoexcited TiO<sub>2</sub>. *J. Phys. Chem. C* **2017**, *121* (13), 7514-7524.
- 66. Ziebel, M. E.; Darago, L. E.; Long, J. R., Control of Electronic Structure and Conductivity in Two-Dimensional Metal-Semiquinoid Frameworks of Titanium, Vanadium, and Chromium. *J. Am. Chem. Soc.* **2018**, *140* (8), 3040-3051.
- 67. Herzberg, G., Molecular Spectra and Molecular Structure. II, Infrared and Raman Spectra of Polyatomic Molecules. D. Van Nostrand Company: Toronto, 1945; Vol. II.
- 68. Li, B.; Leng, K.; Zhang, Y.; Dynes, J. J.; Wang, J.; Hu, Y.; Ma, D.; Shi, Z.; Zhu, L.; Zhang, D.; Sun, Y.; Chrzanowski, M.; Ma, S., Metal–Organic Framework Based Upon the Synergy of a Brønsted Acid Framework and Lewis Acid Centers as a Highly Ffficient Heterogeneous Catalyst for Fixed-Bed Reactions. *J. Am. Chem. Soc.* **2015**, *137* (12), 4243-4248.
- 69. Knoezinger, H.; Krietenbrink, H., Infrared Spectroscopic Study of the Adsorption of Nitriles on Aluminium Oxide. Fermi Resonance in Coordinated Acetonitrile. *Journal of the Chemical Society, Faraday Transactions 1: Physical Chemistry in Condensed Phases* **1975**, 71, 2421-2430.
- 70. Biesinger, M. C., Advanced Analysis of Copper X-Ray Photoelectron Spectra. *Surf. Interface Anal.* **2017**, *49* (13), 1325-1334.
- 71. Poulston, S.; Parlett, P. M.; Stone, P.; Bowker, M., Surface Oxidation and Reduction of CuO and Cu<sub>2</sub>O Studied Using XPS and XAES. *Surf. Interface Anal.* **1996**, *24* (12), 811-820.
- 72. Seah, M. P., The quantitative analysis of surfaces by XPS: A review. *Surf. Interface Anal.* **1980**, *2* (6), 222-239.
- 73. Ko, M.; Mendecki, L.; Eagleton, A. M.; Durbin, C. G.; Stolz, R. M.; Meng, Z.; Mirica, K. A., Employing Conductive Metal-Organic Frameworks for Voltammetric Detection of Neurochemicals. *J. Am. Chem. Soc.* **2020**.
- 74. Aubrey, M. L.; Kapelewski, M. T.; Melville, J. F.; Oktawiec, J.; Presti, D.; Gagliardi, L.; Long, J. R., Chemiresistive Detection of Gaseous Hydrocarbons and Interrogation of Charge Transport in Cu[Ni(2,3-pyrazinedithiolate)<sub>2</sub>] by Gas Adsorption. *J. Am. Chem. Soc.* **2019**, *141* (12), 5005-5013.
- 75. Meng, Z.; Stolz, R. M.; Mendecki, L.; Mirica, K. A., Electrically-Transduced Chemical Sensors Based on Two-Dimensional Nanomaterials. *Chem. Rev.* **2019**, *119* (1), 478-598.



ToC: 8.47 cm x 4.63 cm